The roasting marshmallows program with IGRINS on Gemini South I: composition and climate of the ultrahot Jupiter WASP-18 b

Brogi, M.; Emeka-Okafor, V.; Line, M.R.; Gandhi, S.N.; Pino, L.; Kempton, E.M.-R.; ... ; Désert, J.-M.

The Astronomical Journal, 165:91 (22pp), 2023 March https://doi.org/10.3847/1538-3881/acaf5c

The Roasting Marshmallows Program with IGRINS on Gemini South I: Composition and Climate of the Ultrahot Jupiter WASP-18 b

Matteo Brogi[1,2,3], Vanessa Emeka-Okafor[1], Michael R. Line[4], Siddharth Gandhi[1,5,6], Lorenzo Pino[7], Eliza M.-R. Kempton[8], Emily Rauscher[9], Vivien Parmentier[10,11], Jacob L. Bean[12], Gregory N. Mace[13], Nicolas B. Cowan[14,15], Evgenya Shkolnik[4], Joost P. Wardenier[11], Megan Mansfield[16,21], Luis Welbanks[4,21], Peter Smith[4], Jonathan J. Fortney[17], Jayne L. Birkby[18], Joseph A. Zalesky[19], Lisa Dang[15], Jennifer Patience[4], and Jean-Michel Désert[20]

[1] Department of Physics, University of Warwick, Coventry, CV4 7AL, UK; matteo.brogi@unito.it
[2] INAF-Osservatorio Astrofisico di Torino, Via Osservatorio 20, I-10025 Pino Torinese, Italy
[3] Dipartimento di Fisica, Università degli Studi di Torino, viaPietro Giuria 1, I-10125, Torino, Italy
[4] School of Earth and Space Exploration, Arizona State University, Tempe, AZ 85281, USA
[5] Centre for Exoplanets and Habitability, University of Warwick, Coventry, CV4 7AL, UK
[6] Leiden Observatory, Leiden University, Postbus 9513, 2300 RA Leiden, The Netherlands
[7] INAF—Osservatorio Astrofisico di Arcetri, Largo Enrico Fermi 5, I-50125 Firenze, Italy
[8] Department of Astronomy, University of Maryland, 4296 Stadium Drive, College Park, MD 20742, USA
[9] Department of Astronomy, University of Michigan, Ann Arbor, MI 48109, USA
[10] Université Côte d'Azur, Observatoire de la Côte d'Azur, CNRS, Laboratoire Lagrange, France
[11] Atmospheric, Oceanic, and Planetary Physics, Clarendon Laboratory, Department of Physics, University of Oxford, Oxford, OX1 3PU, UK
[12] Department of Astronomy and Astrophysics, University of Chicago, 5640 South Ellis Avenue, Chicago, IL 60637, USA
[13] Department of Astronomy, University of Texas at Austin, 2515 Speedway, Austin, TX, USA
[14] Department of Earth & Planetary Sciences, McGill University, 3450 rue University, Montréal, QC, H3A 0E8, Canada
[15] Department of Physics, McGill University, 3600 rue University, Montréal, QC, H3A 2T8, Canada
[16] Steward Observatory, University of Arizona, Tucson, AZ 85715, USA
[17] Department of Astronomy and Astrophysics, University of California, Santa Cruz, CA 95064, USA
[18] Astrophysics, University of Oxford, Denys Wilkinson Building, Keble Road, Oxford, OX1 3RH, UK
[19] Department of Astronomy, University of Texas at Austin, 2515 Speedway, Austin, TX 78712, USA
[20] Anton Pannekoek Institute for Astronomy, University of Amsterdam, Science Park 904, 1098 XH Amsterdam, The Netherlands
Received 2022 September 30; revised 2022 December 17; accepted 2022 December 29; published 2023 February 8

Abstract

We present high-resolution dayside thermal emission observations of the exoplanet WASP-18 b using IGRINS on Gemini South. We remove stellar and telluric signatures using standard algorithms, and we extract the planet signal via cross-correlation with model spectra. We detect the atmosphere of WASP-18 b at a signal-to-noise ratio (S/N) of 5.9 using a full chemistry model, measure H_2O (S/N = 3.3), CO (S/N = 4.0), and OH (S/N = 4.8) individually, and confirm previous claims of a thermal inversion layer. The three species are confidently detected ($>4\sigma$) with a Bayesian inference framework, which we also use to retrieve abundance, temperature, and velocity information. For this ultrahot Jupiter (UHJ), thermal dissociation processes likely play an important role. Retrieving abundances constant with altitude and allowing the temperature–pressure profile to adjust freely results in a moderately super-stellar carbon-to-oxygen ratio ($C/O = 0.75^{+0.14}_{-0.17}$) and metallicity ($[M/H] = 1.03^{+0.65}_{-1.01}$). Accounting for undetectable oxygen produced by thermal dissociation leads to $C/O = 0.45^{+0.08}_{-0.10}$ and $[M/H] = 1.17^{+0.66}_{-1.01}$. A retrieval that assumes radiative–convective–thermochemical equilibrium and naturally accounts for thermal dissociation constrains $C/O < 0.34$ (2σ) and $[M/H] = 0.48^{+0.33}_{-0.29}$, in line with the chemistry of the parent star. Looking at the velocity information, we see a tantalizing signature of different Doppler shifts at the level of a few kilometers per second for different molecules, which might probe dynamics as a function of altitude and/or location on the planet disk. Our results demonstrate that ground-based, high-resolution spectroscopy at infrared wavelengths can provide meaningful constraints on the compositions and climate of highly irradiated planets. This work also elucidates potential pitfalls with commonly employed retrieval assumptions when applied to the spectra of UHJs.

Unified Astronomy Thesaurus concepts: Exoplanet atmospheres (487); Exoplanet atmospheric composition (2021); Exoplanet atmospheric dynamics (2307); Exoplanet atmospheric structure (2310); High resolution spectroscopy (2096); Infrared spectroscopy (2285)

1. Introduction

Atmospheric characterization of the exoplanet population provides insight into the mechanisms that drive planetary climate, atmospheric chemical processes and transitions, and planet formation processes (Madhusudhan 2019; Zhang 2020). Transit spectroscopy provides an avenue for measuring diagnostic quantities, such as vertical/horizontal temperature structure and atmospheric composition (volume mixing ratios

[21] NHFP Sagan Fellow.

of individual molecules and atoms/ions) that enable understanding of these critical mechanisms, processes, and transitions (Seager 2010; Madhusudhan 2018; Guillot et al. 2022), especially if such measurements exist over a large sample of planets (Welbanks et al. 2019; Baxter et al. 2020; Mansfield et al. 2021).

Most of the spectroscopic observations either during transit or secondary eclipse use space-based platforms like Hubble Space Telescope (HST) and Spitzer (and currently James Webb Space Telescope (JWST)) with low-to-moderate spectral resolution ($R \sim 50$–1000) or photometry-based instruments (primarily HST WFC3/Space Telescope Imaging Spectrograph (STIS) and Spitzer IRAC; Sing et al. 2016; Guillot et al. 2022). A complementary approach to space-based transit spectroscopy is ground-based time-series with high-resolution cross-correlation spectroscopy (HRCCS; Snellen et al. 2010; Birkby 2018). HRCCS utilizes the planetary orbital Doppler shift of large numbers of molecular lines attainable at high spectral resolutions ($R \gtrapprox 15{,}000$) to disentangle the planetary atmosphere signal from telluric and stellar contaminants. The high spectral resolution is particularly sensitive to the presence of molecular and atomic line absorbers as well as to temperature gradients (Brogi & Birkby 2021). Leveraging this sensitivity, Brogi & Line (2019) showed that quantitative constraints on the key diagnostic quantities—the vertical temperature structure (temperature versus pressure, TP) and gas volume mixing ratios—could be retrieved directly from these types of data (e.g., with the CRIRES instrument on the Very Large Telescope (VLT)) with precision potentially exceeding that achieved when applying similar methods to HST and Spitzer transit observations.

Motivated by the potential for HRCCS observations with modern instruments to provide ultraprecise atmospheric temperature and absolute abundance constraints, Line et al. (2021) leveraged the broad, simultaneous wavelength coverage (1.43–2.42 μm) and high spectral resolution ($R \approx 45{,}000$) of IGRINS (Immersion GRating INfrared Spectrometer; Park et al. 2014; Mace et al. 2018) on Gemini South (GS; 8.1 m) to observe the hot Jupiter WASP-77 Ab (1740 K, 1.36 day period, 1.21 R_J, 1.76 M_J). With a single (4.7 hr) continuous observation of the pre-eclipse phases ($0.32 < \phi < 0.47$, where $\phi = 0$ is a transit and $\phi = 0.5$ is a secondary eclipse), Line et al. (2021) were able to obtain precise constraints on both the TP and on the volume mixing ratios of the dominant carbon and oxygen bearing gases, CO and H_2O ($\pm$0.1–0.2 dex). These CO and H_2O constraints enabled precise metallicity (quantified by the sum of C and O relative to solar, $\pm$0.14 dex) and carbon-to-oxygen ratio constraints (C/O, $\pm$0.08), key diagnostics that link planetary atmospheres to their formation history.

Building upon the successful atmospheric characterization performance of IGRINS on GS shown by Line et al. (2021), we embark on an IGRINS survey (see Figure 1) to measure the thermal emission from the dayside hemisphere of a population of over a dozen hot- to ultrahot Jupiters (UHJs). The goals of the program are to (1) determine the vertical temperature profiles as a function of planetary gravity and stellar influx (equilibrium temperature) and (2) assess the dispersion in the intrinsic elemental inventory of C and O. In this manuscript we present our first results of our survey for the UHJ WASP-18 b (Hellier et al. 2009).

WASP-18 b is a well-studied (Maxted et al. 2013; Wong et al. 2020) transiting UHJ, owing to its high equilibrium temperature (2400 K), short orbital period (0.94 day), favorable transit depth (1.2%, $R_P = 1.191\,R_J$, $R_S = 1.26\,R_\odot$), and bright host star ($V = 9.27$ mag, $K = 8.13$ mag, $T_{eff} = 6400$ K, spectral type F7).[22] The high gravity ($\log g = 4.35$ and $M_P = 10.5\,M_J$) is more akin to those of brown dwarfs rather than "typical" transiting planets, which may preclude it from transmission spectroscopy. However, numerous HST orbits and Spitzer hours have gone into characterizing its thermal emission either through secondary eclipses (Nymeyer et al. 2011; Sheppard et al. 2017; Arcangeli et al. 2018) or phase curve spectrophotometry (Maxted et al. 2013; Arcangeli et al. 2019). The measured hot dayside ($\sim$2900 K), relatively cool nightside ($\lesssim$1500 K), and small eastward phase curve peak offset ($\sim$5°) suggest relatively inefficient day-to-night heat transport, in line with predictions for planets in this temperature range (Iro et al. 2005; Perez-Becker & Showman 2013).

More intriguing are the mixed conclusions regarding the atmospheric composition. Sheppard et al. (2017) analyzed secondary eclipse observations with HST WFC3-G141 and four Spitzer IRAC channels combined with an atmospheric temperature and abundance retrieval analysis (Madhusudhan et al. 2011). They found a high mixing ratio of CO ($\approx$10%–40%, driven by the Spitzer 4.5/3.6 μm flux ratio) and an upper limit on the water abundance (due to the featureless HST WFC3-G141 spectrum), leading to the inference of high metallicity ($\approx$100–700 $\times$ solar) and high C/O ($\approx$1). Such an extreme composition is largely at odds with expectations for the compositions of Jovian-like worlds (Madhusudhan et al. 2014; Thorngren et al. 2016). An independent analysis of the same data set (Arcangeli et al. 2018), but with a different modeling strategy, found an approximately solar composition atmosphere. The key differences between the analyses were primarily model driven. The latter assumed a more physically self-consistent model that included the effects of both water thermal dissociation and H-bound–free/free–free continuum opacity, both of which, along with CO, are expected to sculpt the near-infrared spectra of UHJs (Arcangeli et al. 2018; Parmentier et al. 2018). Both works concluded that the dayside thermal structure was "inverted" (rising temperature with altitude), as predicted (Hubeny et al. 2003; Fortney et al. 2008). Gandhi et al. (2020b) provided yet another independent modeling analysis of various versions of the aforementioned data sets and a hierarchy of minimal-assumption retrieval models to conclude that the published data are largely uninformative and possibly drive the composition toward unphysical solutions.

Given the current atmospheric composition ambiguity of this keystone UHJ, more observations are needed to disentangle the key physical processes and composition. Here, we present an independent analysis of this planet with a different but complementary set of data. Furthermore, WASP-18 b's perplexing atmosphere and favorable observability is why it is included as one of three planets observed in the JWST Transiting Early Release Science Program (secondary eclipse with NIRISS SOSS; Bean et al. 2018).

Next we describe our observations and data reduction, followed by our molecular detections and atmospheric abundance and temperature retrieval results placed within the context of the aforementioned space-based observations.

[22] https://www.astro.keele.ac.uk/jkt/tepcat/planets/WASP-018.html

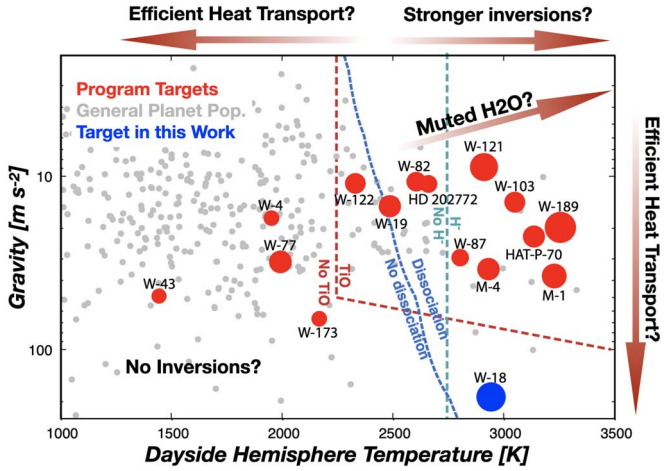

Figure 1. Summary of the Roasting Marshmallows dayside thermal emission HRCCS survey with IGRINS on GS. The key goals are to identify trends in composition and thermal structure over a wide range of stellar irradiation (equilibrium temperature) and planetary mass (gravity). The red circles are the proposed targets and blue is WASP-18, the focus of this work. The symbol size is proportional to the relative emission S/N for each target (e.g., Kempton et al. 2017), scaled to WASP-77 Ab (Line et al. 2021). Qualitative temperature–gravity locations of key atmospheric transitions (onset of the major inversion-causing species TiO/VO and the molecular thermal dissociation transition) are shown as dashed lines (based upon Parmentier et al. 2018). Broad questions are also indicated in the appropriate regions of parameter space. W = WASP, M = MASCARA.

2. Observations and Initial Reduction

We observed WASP-18 b on 2021 September 25 with IGRINS on GS as part of the 117 hr Large-and-Long Program, "Roasting Marshmallows: Disentangling Composition & Climate in Hot Jupiter Atmospheres through High-Resolution Thermal Emission Cross-Correlation Spectroscopy" (GS-2021B-LP-206, PI M. Line, see Figure 1). A continuous sequence of 57 AB pairs (in an AB-BA nodding pattern, 100 s exposure per AB pair) were obtained over a course of 2.85 hr covering the pre-eclipse orbital phases ($0.326 < \phi < 0.452$), which are primarily sensitive to the dayside hemisphere thermal emission. Here orbital phases were computed by using the time of midtransit and orbital period provided in Shporer et al. (2019). We achieved per-resolution element signal-to-noise ratios (S/Ns) between 150 and 290 per AB pair depending on order, comparable to the WASP-77 Ab observations of Line et al. (2021). The initial data reduction (optimal extraction, wavelength calibration) is performed by the IGRINS instrument team using the IGRINS Pipeline Package (Lee & Gullikson 2016; Mace et al. 2018). As described by Line et al. (2021), we perform an additional refinement of the pixel–wavelength solution to correct for the ±0.2 pixel (±0.46 km s^{-1}) shifts measurable throughout the night (see Figure 2). We discard 12 orders heavily contaminated by telluric lines and/or with very low instrumental throughput, namely the wavelength ranges <1.44, 1.79–1.95, and >2.42 μm. Furthermore, we remove the first and last 100 pixels from each order to discard spectral regions with negligible flux due to the instrumental blaze function.

Following standard practice, the spectra are packaged into an $N_{ord} \times N_{int} \times N_{pix}$ data cube for subsequent analyses, where $N_{ord} = 42$ is the number of spectral orders, $N_{int} = 57$ is the number of spectra, and $N_{pix} = 1848$ the number of spectral channels after the order selection and edge trimming described above.

In ground-based HRCCS observations, the dominant spectral features from telluric and stellar lines must be removed from the spectral sequence. As these contaminants are stationary (or quasi-stationary) in wavelength, it is possible to model them as time-correlated trends in common between spectral channels.

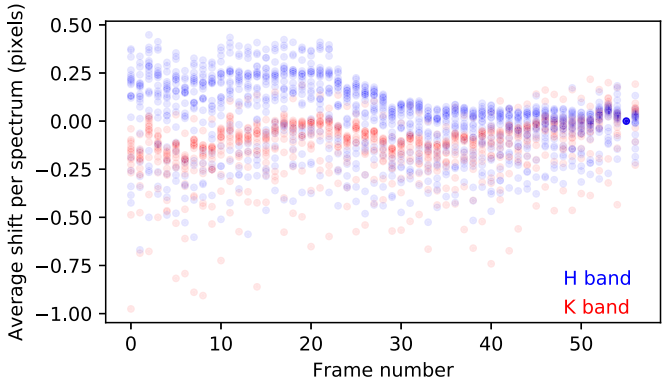

Figure 2. Measured shifts (in pixels) vs. time of the IGRINS spectral sequence for orders in the *H* band (blue, one dot per order) and in the *K* band (red dots).

Following de Kok et al. (2013) and Line et al. (2021) we use the singular value decomposition (SVD) method in the time domain (TD) to isolate the dominant trends (a.k.a. components) and subtract their best-fit linear combination to correct for the observed flux variations. We remove five components in this case, but the result is very weakly dependent on the number of components within the tested range (3–11 components). We apply three additional steps compared to Line et al. (2021):

1. For each order, we exclude spectral channels with flux levels less than 2% of the median value computed across wavelength. This step prevents the SVD algorithm from focusing on decomposing noisy spectral channels where telluric lines are close to saturation. Depending on the order, we discard between 0% and 8.6% of the data.
2. For each order, we mask spectral channels with strong residuals after subtracting the SVD fit, with a dynamic threshold dependent on the number of spectral channels available per order, and ranging between 3.24 and 3.27× the mean standard deviation of the residuals.[23] The additional number of spectral channels masked is typically below 1%, and at most 2.7%. Over the 42 orders analyzed, 1.9% of the data is excluded from subsequent steps due to the pre- and post-SVD masking.
3. We apply a high-pass filter to the residuals, by convolving each spectrum with a Gaussian kernel of FWHM = 80 pixels, and subtracting the smoothed spectrum. This step removes any broadband correlated noise along the wavelength axis (the N_{pix} dimension).

We note that in the literature (e.g., Giacobbe et al. 2021) there are alternative versions of SVD, or more generally principal component analysis (PCA) methods, used to clean high-resolution spectra from telluric and stellar contaminants. In Appendix A, we show that the signal detected is robust against the choice of such de-trending algorithm, i.e., retrieved velocities and scaling parameters are consistent within 1σ.

[23] Given N_{ch} spectral channels, the threshold is computed as via `scipy.stats.norm.isf` as the inverse survival function of a normal distribution with argument $1/N_{ch}$.

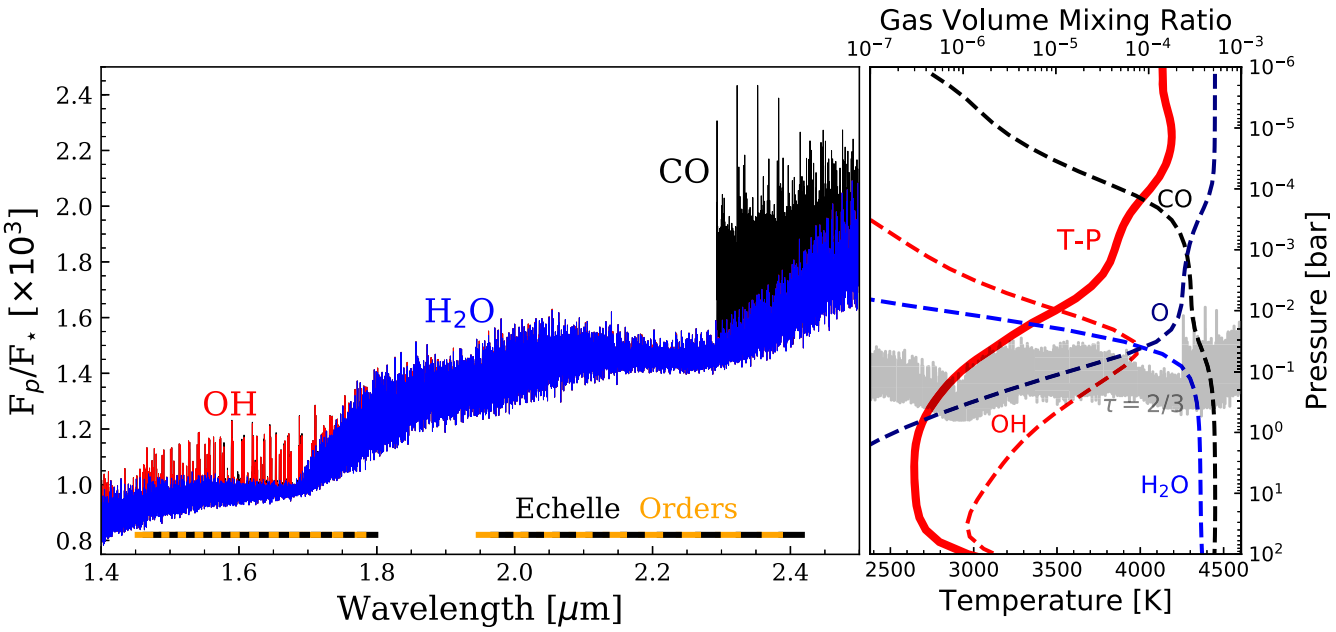

Figure 3. Components of the spectrum that contribute to the observed signal. The template spectrum is a result of a 1× solar composition atmosphere in the 1D-RCTE, assuming a redistribution factor of 2.35 (based upon the trend of Parmentier et al. 2021). The dominant absorbers are H_2O, OH, and CO. Starting with H_2O (on top of an H-bound–free/free–free continuum), the other gases are sequentially added to illustrate their contribution to the total spectrum. The right panel shows the atmospheric structure (gas volume mixing ratio profiles for H_2O, OH, CO, and O as dashed lines and the temperature–pressure profile in solid red) from the 1D-RCTE model. The atomic oxygen (O) profile is also shown to illustrate its role in the total elemental oxygen inventory. Also shown is the $\tau = 2/3$ surface (in gray) used to identify the pressure levels sensed by the observations—between 1 and 0.01 bar. This suggests that the observations are sensitive to the region where the mixing ratio profiles change rapidly due to thermal dissociation as a result of the rapidly increasing temperature with altitude.

3. Molecular Detections with Cross-correlation

We perform an initial search for molecular absorbers in the atmosphere of WASP-18 b by comparing our data to template spectra derived from planet-specific 1D radiative–convective–thermochemical equilibrium (1D-RCTE) models (Arcangeli et al. 2018; Piskorz et al. 2018; Mansfield et al. 2021) at solar composition post-processed at an $R = 250{,}000$ and subsequently convolved to a Gaussian instrumental profile corresponding to an $R = 45{,}000$ (Figure 3). We look for the signatures of H_2O, CO, and OH as they are the primary species expected to be present over the IGRINS passband for any reasonable atmospheric composition. We also consider the possible presence of Si I, Ca I, and FeH, all of which possess lines over the IGRINS passband. However, when considering these in the context of the WASP-18 b dayside conditions via the 1D-RCTE model, Si I presents no lines and the lines from Ca I and FeH are relatively weak so that they do not significantly impact the cross-correlation.

3.1. Detections via Cross-correlation

We obtain a clear detection of the atmosphere of WASP-18 b when cross-correlating with the 1D-RCTE model including all (H_2O+CO+OH) the gases, at an S/N = 5.9. This is shown in Figure 4 as a function of rest-frame velocity and planet maximum radial velocity. The dotted lines indicate the predicted planet position using the literature orbital solution from Shporer et al. (2019) and a systemic velocity of $V_{sys} = 4.1 \pm 0.6$ km s^{-1} (Gaia Collaboration et al. 2018). As standard in the literature, the quoted S/N is computed by dividing the peak cross-correlation by the standard deviation of the noise away from the peak. To mitigate the somewhat subjective choice of noise samples, we fit the distribution of

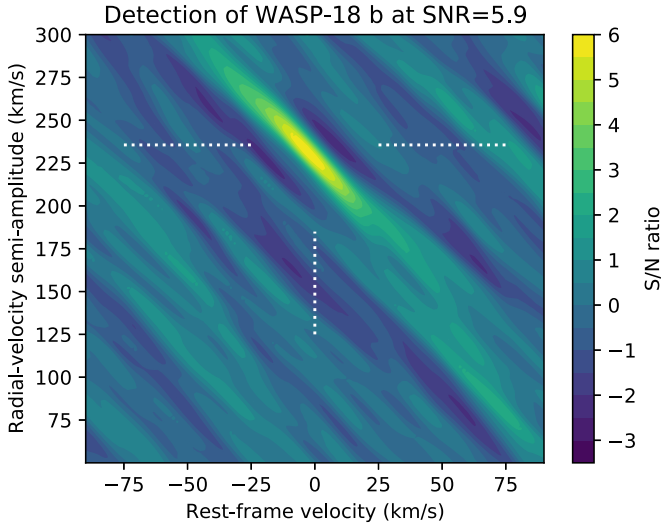

Figure 4. Detection of the thermal emission spectrum of WASP-18 b when cross-correlating with the 1D-RCTE model described in Section 3.1. The planet is detected at an S/N of 5.9, and at a position in velocity space consistent with the literature solution for the orbit and the velocity of the system (white dotted lines).

cross-correlation values with a Gaussian profile and use the Gaussian σ as a proxy for noise.

Figure 5 (top panel) summarizes our search for each species via cross-correlation. We tentatively detect H_2O (S/N = 3.3) and we obtain firmer detections of OH (S/N = 4.8) and CO (S/N = 4.0), the latter by restricting the analysis to the four orders of the K band longward of 2.29 μm where the 2–0 rovibrational band-head of CO begins. When using a template that includes all three species at their predicted equilibrium abundances, the detection S/N increases to 6.

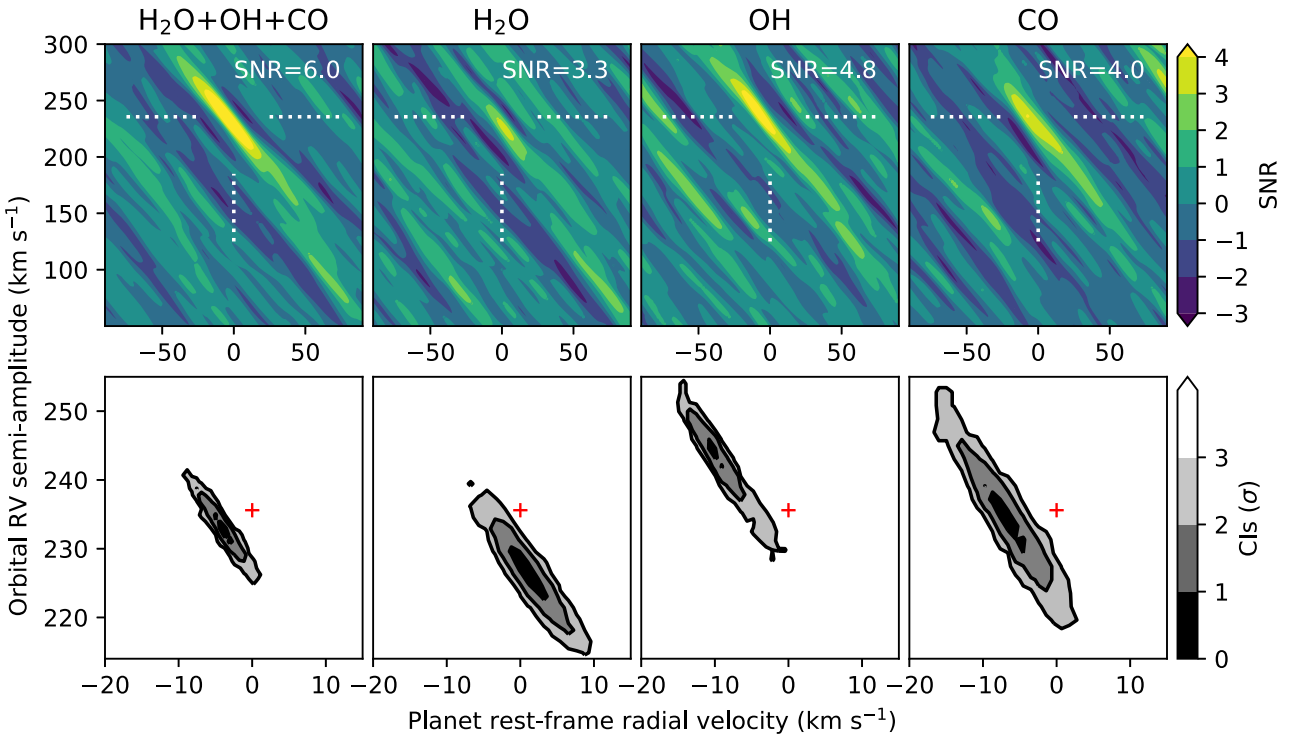

Figure 5. Top row: cross-correlation maps of the species detected in the atmosphere of WASP-18 b using the model spectra shown in Figure 3. The S/Ns are computed by dividing the peak value by the standard deviation away from the peak (Section 3.1). The literature solution for the planet velocity is indicated with white dashed lines. Bottom row: CIs for the same models as the top row, obtained via the likelihood framework and a three-parameter Markov Chain Monte Carlo model as described in Section 3.2. Each species is detected above the 3σ level. Visual comparison of the offset contours to the literature solution (red cross) indicates the potential atmospheric dynamics as a function of species (Section 5.3).

Unsurprisingly, we do not detect neutral Ca, Si, or FeH individually nor do these species significantly lower the overall detection significance when included in the analysis (Figure 4). We also note that the 1D-RCTE models tested all present a thermal inversion layer, and thus the positive correlation seen in Figures 4 and 5 suggests that an inverted atmosphere is indeed consistent with these data.

3.2. Detections with the Likelihood Framework

In Figure 5 (bottom panel), we show the velocity confidence intervals (CIs) derived through the likelihood framework of Brogi & Line (2019) for the same set of models presented in Section 3.1. In order to estimate properly the velocity CIs in such a framework, it is important to match the overall line depth in addition to their position, because changes in line depth produce a stretch of the log-likelihood function. Therefore, we add a global log-scaling factor of $\log(a)$ in addition to the two velocities and sample the 3D posteriors via the Python `emcee` package, with priors listed in the top three rows of Table 1, and with the atmospheric spectra fixed to the 1D-RCTE spectrum described in Section 3. When using the likelihood framework, it is imperative to reproduce the effects of the data analysis on each model generated by the parameter estimation sampler. Such model reprocessing is implemented by multiplying the SVD fit obtained in Section 2 by the appropriate Doppler-shifted, scaled model, and by reapplying the SVD algorithm to the injected model sequence with the same number of components and mask as for the observed data. In this analysis, applying a high-pass filter to the reprocessed model does not noticeably change the derived CIs, and therefore we skip this step to reduce the computational times.

Table 1
Description of the Retrieved Parameters and their Prior Ranges

Parameter	Description	Prior
K_P	planet orbital velocity	200–300 km s^{-1}
V_{rest}	excess rest-frame velocity	−30 to 30 km s^{-1}
$\log(a)$	model multiplicative scale factor	−1 to 1
$\log(\gamma_1)$	vis-to-IR opacity	−3 to 3
$\log(\kappa_{IR})$	IR opacity	−3 to 0.5 (cgs)
T_{irr}[a]	irradiation temperature	1500–4500 K
H_2O, CO, OH	log gas volume	−12 to 0
FeH, HCN, Ca I	mixing ratios	
H-	for bound–free cont.	−15 to −1
H^*e^-	for free–free cont.	−20 to −1

Notes. All priors are assumed uniform between the bounds given. Variables correspond to the labeling in the corner plot shown in the Appendix.
[a] Irradiation temperature is really a measure of the equivalent dayside temperature.

While detection significance is not measurable via a likelihood ratio, we can look at the drop in significance between the best-fit velocities and the rest of the posteriors as a proxy for it. For the three species detected in Section 3.1, the peak likelihood is favored at more than 4σ over any other signal, demonstrating the superior performance of the likelihood framework compared to pure cross-correlation in localizing the signature of molecular species in velocity–amplitude space. This is in line with the expectation that the likelihood of Brogi & Line (2019) uses not only the information about the line position, but also about the line shape and depth. Despite the higher sensitivity, no bound

posterior is obtained when testing the models containing Ca, Si, and FeH.

The results from the likelihood framework are suggestive of different dynamics probed by the three detected species. This effect is visible in Figure 5 as a shift in the best-fit rest-frame velocities for H_2O, CO, and OH. We further discuss these velocity shifts in Section 5.

4. Temperature and Abundance Retrieval Analysis

The above search for molecular species provides qualitative insights into the atmospheric composition. In order to obtain quantitative constraints on the molecular abundances and temperature profile (and subsequent products like the atmospheric metallicity and C/O ratio) we must perform an atmospheric retrieval. Following Line et al. (2021) and Kasper et al. (2021, 2023), we applied the Brogi & Line (2019) cross-correlation-to-log-likelihood retrieval framework to derive the molecular volume mixing ratios and the vertical temperature structure. While going through the retrieval process we gleaned critical insights into the performance of two HRCCS retrieval frameworks: "free retrievals" and "1D-RCTE grid retrievals" ("gridtrieval"). The processes of interpreting the free-retrieval results in Section 5 caused us to question the applicability of free retrievals to UHJs. This then led us to employ the 1D-RCTE-based "gridtrieval" method described in Section 5.2. Below, and in the following sections, we document our path chronologically, the assumptions we tested, and ultimately the results upon which we settle.

We begin the retrieval process with the basic `CHIMERA` free-retrieval (Line et al. 2013; Kreidberg et al. 2015) paradigm which assumes constant-with-altitude gas mixing ratios and uses the three-parameter Guillot (2010) parameterization for the TP profile. We start with this method/paradigm as it worked well for the cooler planet, WASP-77Ab, in Line et al. (2021). The retrieval parameters specific to our analysis here and their prior ranges are given in Table 1. A more detailed description of the high-resolution GPU-based radiative-transfer method, including opacity sources[24] and log-likelihood implementation within `pymultinest` (Feroz et al. 2009; Buchner et al. 2014) is given in Line et al. (2021).

Within the free-retrieval paradigm, we perform a series of exploratory experiments with various assumptions in order to test the robustness of the results. Figures 6 and 7 summarize these results compared with a battery of WASP-18 b-specific 1D-RCTE[25] models (Arcangeli et al. 2018; Mansfield et al. 2021) of different compositions. Table 2 gives the numerical values for the 68% CI for each parameter under each scenario. The full posteriors for each scenario are given as corner plots in Appendix C.

4.1. Fiducial Retrieval

Under the fiducial setup ("Fiducial" in Figures 6 and 7 and in Table 2), we retrieve for all of the parameters with the given priors shown in Table 1 on the full data sequence. We obtain bounded constraints on the volume mixing ratios of H_2O, CO, and OH and upper limits on all of the other species we explored (Table 2). These results are consistent with the detections in the cross-correlation analysis (Section 3). As in Line et al. (2021), we attempt to constrain the $^{13}CO/^{12}CO$ isotopologue ratio, but arguably due to the lower S/N of the detection we can only place an uninformative upper limit on their ratio (see Appendix Figure 13). The top panel of Figure 6 shows the gas mixing ratio constraints (95% CIs shown with the shaded region) on H_2O, CO, and OH from this setup compared to those predicted by series of 1D-RCTE[26] models of differing compositions (via metallicity,[27] [M/H], and C/O). The retrieved mixing ratios are consistent with physically plausible combinations of these species and with metallicities between ∼solar ([M/H] = 0.0) and <30× solar ([M/H] = 1.5). The constraints on water rule out the higher metallicities, whereas the constraints on OH tend to prefer metallicities elevated above solar. The CO constraints are consistent with a wide range of metallicities. We also show the impact of the elemental C/O on the 1D-RCTE profiles (as dashed lines) under an [M/H] = 0.5. The "high" C/O (0.9) scenario is in tension with both the water and OH abundances. Low C/O values (0.1) have little influence on the 1D-RCTE H_2O and OH abundance profiles, but do impact CO directly. In Section 5 we discuss a more detailed elemental abundance analysis. Here we simply aimed to illustrate that regions of the retrieved gas mixing ratios and their combinations are chemically plausible under a wide range of elemental compositions.

These data also provide coarse constraints on the vertical temperature profile, specifically, the visible-to-IR opacity, $\log(\gamma_v)$, which governs the atmospheric temperature gradient; values of $\log(\gamma_v) < 0$ produce decreasing temperatures with decreasing pressure, 0 produces isothermal atmospheres, and >0 results in temperatures that increase with decreasing pressure, or inversions. Our retrieved median $\log(\gamma_v)$ is larger than zero by more than 3σ (see Appendix Figure 13), a clear indication of a temperature structure with a thermal inversion.

We obtain only lower limits on the retrieved irradiation temperature ($T_{\rm irr}$), with most of the posterior above the planet's equilibrium temperature of $T_{\rm eq} \approx 2400$ K. As defined in footnote 24, we can relate the retrieved irradiation temperature back to a "heat redistribution" efficiency, assuming that the retrieved irradiation temperature represents the dayside temperature. The maximum redistribution efficiency of 2.67 would only allow dayside temperatures up to 3065 K for WASP-18 b. With the posterior pushing to the edge of the prior at 4500 K, our "Fiducial" model thus retrieves nonphysical temperatures

[24] Transition and broadening information are taken from a variety of sources and is used to precompute cross sections on a TP–wavenumber grid. The H_2O (Polyansky et al. 2018) and FeH (Bernath 2020) data are sourced from the ExoMol project (https://www.exomol.com/data/molecules/; Tennyson et al. 2020) and the cross sections are generated using the methods described by Gharib-Nezhad et al. (2021). We use HELIOS-K (https://helios-k.readthedocs.io/en/latest/; Grimm et al. 2021) to generate the OH and CO cross sections drawn from the HITEMP (https://hitran.org/hitemp/) database (Rothman et al. 2010; Gordon et al. 2022). The HCN (Barber et al. 2013; Tennyson et al. 2020) cross sections are also generated with HELIOS-K. Finally, we use the Kurucz & Bell (1995) atomic line information (https://lweb.cfa.harvard.edu/amp/ampdata/kurucz23/sekur.html) to compute the atomic cross sections using a custom routine and the H-free–free/bound–free cross sections are generated using the methods described by John (1988).

[25] For 1D-RCTE models one has to assume a "heat redistribution" (Fortney et al. 2005) to derive the mean dayside hemispheric properties—a variable that multiplies the incident stellar flux. We define redistribution as $(T_{\rm day}/T_{\rm eq})^4$ with $T_{\rm day}$ the dayside temperature and $T_{\rm eq}$ the equilibrium temperature. A value of unity implies $T_{\rm day} = T_{\rm eq}$ and a value of two implies $T_{\rm day} = 2^{1/4}T_{\rm eq}$. The maximum physical value is 2.67 (Cowan & Agol 2011; Arcangeli et al. 2019).

[26] Here, we assume a redistribution factor of 2.2, consistent with the "nightside clouds" trend of Parmentier et al. (2021). The C/O is assumed to be 0.5 unless otherwise stated.

[27] We use the Lodders et al. (2009) elemental abundances as our solar reference. [M/H] = 0, 1, 2 represent 1, 10, 100× the solar elemental values, respectively.

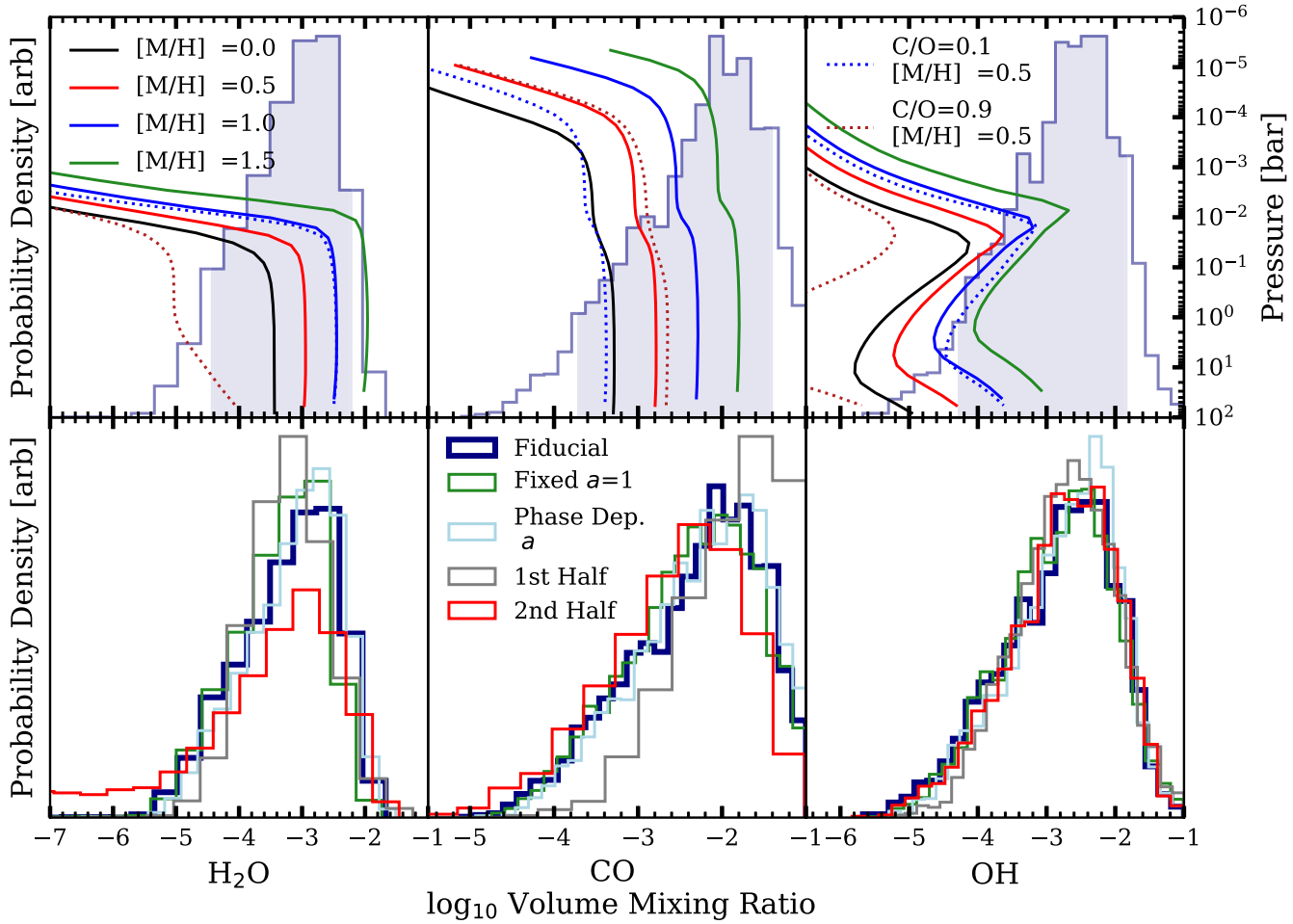

Figure 6. Summary of the free-retrieval results for the constrained species, H_2O, CO, and OH. Top row: marginalized gas mixing ratio histograms (95% CI shown as shaded region) under the "Fiducial" scenario described in Section 4.1 compared to a series of variable-composition self-consistent 1D-RCTE model abundance profiles (see footnotes 24–26). The retrieved abundances are consistent with a wide range of metallicities, but their combination can rule out self-consistent combinations of gases at high C/O. Bottom row: summarizes the impact of the free-retrieval assumptions on the marginalized gas mixing ratio histograms (see Sections 4.2 and 4.3). These assumptions appear to have a minimal quantitative impact on the gas volume mixing ratios.

for this planet, which we believe is due to the known correlation with the scaling factor a.

The retrieved log-scaling factor is not bounded in this "Fiducial" retrieval run, which might indicate the inability of the model to reproduce both the shape and the depth of spectral lines in the presence of thermal dissociation. With a low retrieved log-scaling factor, the line amplitude has to be compensated by an increase in the planet irradiation temperature and/or in the lapse rate.

We also observe a degeneracy between the $\log(\kappa_{\rm IR})$ parameter, which controls the "vertical pressure shift" in the TP profile via the mapping between optical depth (τ) and pressure ($\tau = \kappa_{\rm IR} P/g$), and gas mixing ratios. As pointed out in past works (Line et al. 2015; Piette & Madhusudhan 2020), increasing the abundances of a gas shifts the "average" $\tau = 2/3$ surface to lower pressures. To maintain a constant temperature gradient over the line-formation pressures, the whole TP profile must "shift up" by increasing $\kappa_{\rm IR}$. While pressure broadening alters the line shape and should thus help "anchoring" the TP profile at a high-enough S/N, at first order or low S/N the above degeneracy is only halted when either a gas abundance or $\kappa_{\rm IR}$ runs up against its prior edge, as can be seen in Appendix Figure 13.

The 95% confidence band resulting from the reconstructed TP profiles, marginalized over all of the aforementioned degeneracies, is shown in the upper left panel ("Fiducial") in Figure 7. The uncertainties are about 1000 K, much larger than those obtained for our previous target, WASP-77 Ab.

We test the sensitivity of the absolute abundances to the scaling factor in Section 4.2, while we discuss the shortcomings of the model and propose an alternative retrieval ("gridtrieval") scheme in Sections 5.1 and 5.2, respectively.

4.2. Phase-dependent and Fixed Scaling Factor

As the daysides of UHJs are anticipated to be much hotter than the nightsides (e.g., Arcangeli et al. 2019), it is not unreasonable to presume that any phase dependency in flux is simply due to a phase-dependent dayside dilution. We observe the more irradiated, and hence hotter, dayside hemisphere closer to secondary eclipse, which progressively becomes "area-diluted" by a cooler, lower flux nightside (which we take to be negligible), at phases closer to quadrature. We parameterize this effect with a phase-dependent scale factor, $\log[a(\varphi)]$, modulated with a cosine function (Burrows et al. 2006), which is 0 at $\varphi = 0$ (midtransit, only nightside visible), and 1 at $\varphi = 0.5$ (mideclipse, full dayside; "Phase Dep. a" in

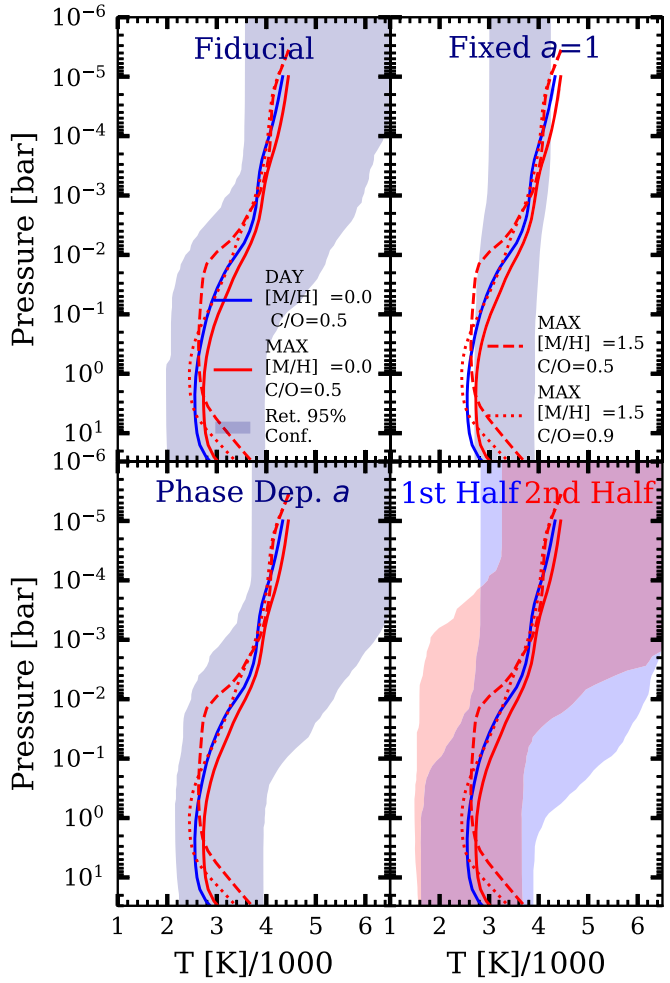

Figure 7. Summary of the retrieved TP profiles and their sensitivity to the various free-retrieval assumption scenarios described in Section 4, indicated at the top. These are summarized with the 95% CIs derived from individual temperature profiles reconstructed from 500 random posterior draws (based upon the $T_{\rm irr}$, $\log(\kappa_{\rm IR})$, and $\log(\gamma_v)$ constraints). We also include select self-consistent 1D-RCTE TP profiles to facilitate comparison. Here, DAY represents a redistributing scaling factor of 2 and MAX is 2.67 (see footnote 23). Despite the wide CIs, the general morphology of the retrieved TP profiles is consistent with the 1D-RCTE predictions (e.g., rising temperature with decreasing pressure).

Figures 6 and 7 and in Table 2), though we still retrieve for a constant multiplicative factor, a, on top of this phase-dependent scaling. Upon doing so, we do not see any meaningful difference in either the abundances (Figure 6, bottom row) or temperature (Figure 7, bottom left) with the "Fiducial" retrieval. The Bayesian evidence difference (bottom row, Table 2) between this and the "Fiducial" scenarios are considered insignificant on Jeffery's scale (Trotta 2008), confirming the lack of meaningful effect.

Lastly, we fix $\log(a) = 0$ ("$a = 1$" in Figures 6 and 7 and in Table 2) to test for any dependence of the measured abundances on the scaling factor. In Section 4.1 we showed that the retrieved scaling factor has a posterior leaning toward the lower edge of the prior. For UHJs we would expect scale factors below unity as the spectral shape we observe is dominated by a locally hotter region on the dayside hemisphere, but the overall flux is decreased due to the "area dilution" from the cooler off-hot-spot regions of the dayside hemisphere. However, a posterior strongly leaning toward $\log(a) = -1$ would imply a reduction of a factor of 10 in the strength of emission lines. Given that at the orbital phases probed the sub-stellar point is still in view and the emission predominantly comes from the planet's dayside, such a small value of a cannot be explained with the dilution argument above. It is therefore worth testing whether such a small scaling factor can impact the abundance measurements. By looking at Table 2 and the bottom row of Figure 6, it is clear that the abundances retrieved with $\log(a) = 0$ are identical to those from the "Fiducial" run within a small fraction of the 1σ CI. Inspecting the other parameters reveals that the change in scaling factor is completely absorbed by the TP profile, which is much shallower in this case to compensate for the larger amplitudes of the spectral lines.

In the next section, we explore the impact of the phase range —which maps to longitude on the planet—on the retrieved properties.

4.3. Phase-resolved Retrieval

In order to explore potential longitudinal variations in composition, temperature, and winds, we split the spectral sequence in half and separately retrieved for each subset. The 1st half covers $0.326 < \phi \leqslant 0.389$ and the 2nd half covers $0.389 < \phi \leqslant 0.452$. The latter half covers more of the irradiated dayside than the former. We show the full posteriors of these runs in the Appendix Figures 16 and 17.

First we focus on the changes on the abundance of the three detected species (H_2O, CO, and OH), shown in the bottom row of Figure 6. These changes are negligible at most, and can be summarized in a lower precision constraint on water (as shown by the posterior tail toward lower abundances in Figure 6, bottom left panel) for the 2nd half—when more of the hot spot is visible—and a very marginal increase in the CO abundance for the 1st half. There is no change in the OH abundance constraints. We do not see any notable shift in the chemistry of the other undetected species. The bottom right panel in Figure 7 compares the reconstructed TP profiles retrieved from each half-sequence. The large uncertainties preclude the identification of any obvious differences, with perhaps a minor shift in pressure. The $\log(\gamma_v)$ constraints (Table 2) from both half-sequences indicate the obvious presence of an inversion.

Finally, we look for shifts in the retrieved $K_{\rm P}$ and $V_{\rm rest}$ as proxies for possible atmospheric dynamics. We retrieve an excess $V_{\rm rest}$ shifting from $-5.2^{+5.9}_{-5.2}$ km s^{-1} for the first half to -11.7 ± 3.2 km s^{-1} for the second half, with the "Fiducial" retrieval sitting somewhat in the middle ($V_{\rm rest} = -7.2^{+2.6}_{-2.3}$ km s^{-1}). However, we note that $V_{\rm rest}$ and $K_{\rm P}$ are highly correlated parameters in emission spectroscopy when just the pre- or post-secondary eclipse phases are observed. In fact, when we explore the 2D posterior in both $V_{\rm rest}$ and $K_{\rm P}$, the solutions from the first and second halves are still consistent at $\sim 1\sigma$. We briefly note here that phase effects measured via HRCCS are different from phase curves measured at low spectral resolution or multiband photometry. Whereas the latter mostly probe changes in the planet's continuum, the former encode changes in the line depth, i.e., they map the temperature difference between the continuum and the line cores. Therefore, we should not necessarily expect HRCCS phase curves to match low-resolution phase curves, particularly when investigating shifts of the maximum amplitude from the sub-stellar point (e.g., van Sluijs et al. 2022).

Table 2
Retrieved Parameters for the Five Retrieval Setups Described in Section 4

Parameter	Units	Fiducial	1st Half	2nd Half	Phase Dep. a	Fixed $a = 1$
$\log_{10} n_{\rm H2O}$	⋯	$-3.13^{+0.66}_{-0.98}$	$-3.21^{+0.62}_{-0.64}$	< -2.01	$-3.03^{+0.62}_{-0.92}$	$-3.28^{+0.62}_{-0.89}$
$\log_{10} n_{\rm CO}$	⋯	> -4.12	> -3.36	> -4.50	> -3.91	> -4.04
$\log_{10} n_{\rm Ca}$	⋯	< -5.13	< -3.96	< -6.67	< -5.02	< -4.54
$\log_{10} n_{\rm FeH}$	⋯	< -6.66	< -5.98	< -6.58	< -6.66	< -6.62
$\log_{10} n_{\rm HCN}$	⋯	< -2.04	< -2.29	⋯	< -1.89	< -2.23
$\log_{10} n_{\rm OH}$	⋯	> -4.74	> -4.20	> -4.61	$-2.63^{+0.63}_{-0.94}$	> -4.55
$[^{13}{\rm CO}/^{12}{\rm CO}]$	⋯	<1.70	<2.12	<1.24	<1.64	<1.58
$\log_{10} n_{\rm H-}$	⋯	< -6.62	< -7.25	< -5.06	< -6.48	< -6.66
$\log_{10} n_{\rm H} n_{e-}$	⋯	⋯	< -2.00	⋯	⋯	⋯
$\log_{10}(\gamma_v)$	⋯	$0.74^{+0.40}_{-0.36}$	$0.74^{+0.55}_{-0.40}$	>0.45	$0.86^{+0.36}_{-0.36}$	$0.17^{+0.06}_{-0.04}$
$\log_{10}(\kappa_{\rm IR})$	⋯	> -2.45	< -0.30	> -2.28	> -2.31	> -2.22
$T_{\rm irr}$	K	>2086	>1791	⋯	>2187	3559^{+288}_{-391}
$K_{\rm P}$	km s^{-1}	$234.6^{+2.9}_{-2.9}$	$232.6^{+6.3}_{-7.4}$	$244.3^{+6.7}_{-5.8}$	$235.1^{+3.0}_{-3.0}$	$234.5^{+2.9}_{-2.7}$
$V_{\rm rest}$	km s^{-1}	$-7.2^{+2.6}_{-2.3}$	$-5.2^{+5.9}_{-5.2}$	$-11.7^{+3.2}_{-3.2}$	$-7.7^{+2.6}_{-2.0}$	$-4.9^{+1.9}_{-1.9}$
$\log_{10}(a)$	⋯	< -0.10	<0.20	< -0.05	< -0.21	⋯
$\Delta \ln \mathcal{Z}$[a]	⋯	0	N/A	N/A	0.59	1.34

Notes. Quoted uncertainties are 1σ intervals for the bounded parameters and 2σ for upper or lower limits. Dashes denote unconstrained parameters.
[a] "Fiducial" minus the given scenario, e.g., $\ln \mathcal{Z}_{\rm Fid.} - \ln \mathcal{Z}$.

5. Discussion

5.1. Deriving the Chemistry of WASP-18 b from Retrieved Abundances

Compared to our pilot study for WASP-77 Ab (Line et al. 2021), the WASP-18 b retrieval struggles to constrain the absolute abundances of the three detected species. In fact, the measured precision of 1 dex or better is being influenced by the prior limit on $\kappa_{\rm IR}$ (e.g., see the $\log_{10}(\kappa_{\rm IR})$ row in Figure 13), rather than being entirely constrained by the data alone. Nevertheless, the correlation between species visible in Appendix Figures 13 to 15 suggests a higher precision in measuring relative abundances, which should help constraining elemental abundance ratios such as C/O.

Here we infer the free-retrieval-based C/O and metallicity of WASP-18 b by counting the total elemental number density arising from each species (Table 2, column "Fiducial"). We then compare the measured chemistry to that of the parent star. Importantly, we do not assume solar composition for WASP-18. As mentioned in footnote 25 we take the solar elemental abundances from Lodders et al. (2009; $({\rm C/O})_\odot = 0.46$). For the star WASP-18, we use the recent abundance study of Polanski et al. (2022), where the abundances are relative to the solar values of Grevesse et al. (2007; A. Polanski 2023, private communication)—similar but not identical to Lodders et al. (2009). Remarkably, the reported stellar C/O of WASP-18 is 0.23 ± 0.05,[28] i.e., significantly lower than the solar value. The stellar metallicity is approximately solar ([M/H] = 0.045).

To compute the planetary C/O and metallicity with the above in mind, we use the following formulae:

$$[{\rm C}\,/\,{\rm O}] = \frac{n_{\rm C}}{n_{\rm O}} = \frac{n_{\rm CO} + n_{\rm HCN}}{n_{\rm CO} + n_{\rm OH} + n_{\rm H2O}}, \quad (1)$$

and

$$[{\rm M}\,/\,{\rm H}] = \log\left\{\frac{2n_{\rm CO} + 2n_{\rm HCN} + n_{\rm OH} + n_{\rm H2O}}{2n_{\rm H2}\,[(n_{\rm O} + n_{\rm C} + n_{\rm N})/n_{\rm H}]_\odot}\right\}, \quad (2)$$

where the numerator in Equation (2) sums over the number densities of all the species containing metals ("M") relative to the assumed hydrogen fraction ($n_{\rm H} = 2n_{\rm H2}$) in the free retrieval.[29] We thus note that $n_{\rm H2}$ in the denominator is different for each posterior sample because it depends on the number densities of all the other gases. For reference, its median value is $n_{\rm H2} = 0.844$. The planetary "M/H" is further normalized to the sum of the solar C/H, O/H, and N/H. We find that the addition of Fe and Ca from the undetected species makes a negligible difference in the measured planet metallicity, but they are still included in the computation of $n_{\rm H2}$.

Figure 8 shows the joint probability for C/O and metallicity. We obtain ${\rm C/O} = 0.75^{+0.14}_{-0.17}$ and $[{\rm M/H}] = 1.03^{+0.65}_{-1.01}$. The C/O is constrained to be less than 1 at the 2σ level but is still markedly super-stellar. The metallicity is also super-stellar, although consistent with stellar values at 2σ. Overall, our free-retrieval-derived elemental abundances are indicative of a planetary atmosphere that is super-stellar in both metallicity and C/O at $>2\sigma$.

There are, however, several shortcomings within the "free-chemistry" retrieval paradigm that might lead to biases—especially in UHJs. First, the strong detection of OH (and correspondingly weaker detection of H_2O) is an indirect confirmation of thermal dissociation. Thermal dissociation will convert H_2O into both OH and atomic O, and these infrared IGRINS observations are not sensitive to the latter. Unaccounted atomic O ($\gtrsim$40% of the total O inventory at $p < 10^{-2}$ bar—Figure 3, right) could potentially produce an upwards bias of any C/O estimates based on Equation (1) alone. If the

[28] We acknowledge the challenges in obtaining stellar C/O ratios (Fortney 2012; Brewer & Fischer 2016). A model-independent analysis (Bedell et al. 2018) of solar neighborhood solar twins suggests that C/Os < 0.4 are unlikely. Furthermore, Kolecki & Wang (2022) find systematically higher C/Os than Polanski et al. (2022) for overlapping stars (though they do not include WASP-18 b in their analysis).

[29] In the free retrieval, the filler gas is assumed to be H_2+He (with $n_{\rm He}/n_{\rm H2} = 0.176$). Certainly this assumption breaks down in UHJs where atomic H dominates. As long as the total H is accounted for, this assumption should not matter for elemental counting purposes.

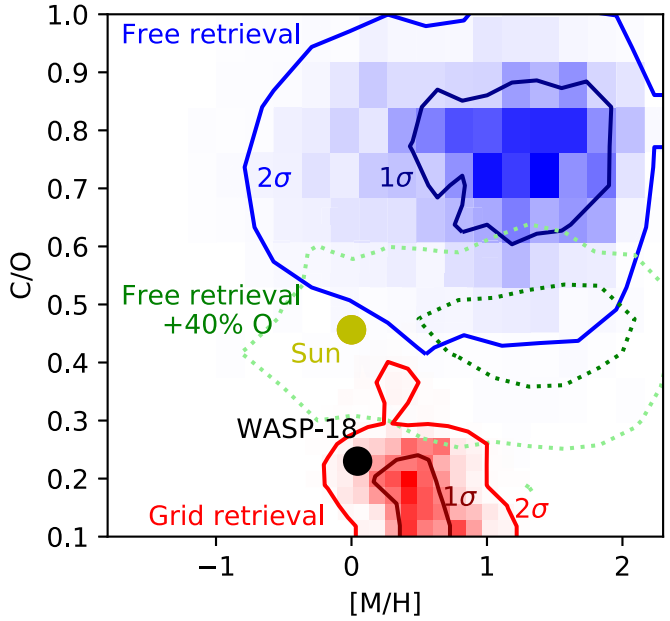

Figure 8. Elemental abundances derived from the free-retrieval gas mixing ratio constraints (blue) vs. the corresponding constraints from the self-consistent, grid-based 1D-RCTE retrieval (red). A correction to the free retrieval accounting for ≈40% atomic oxygen (non-detectable) is shown with the green dotted lines. Elemental values for the star, WASP-18, are shown as the black dot (Polanski et al. 2022) and those for the Sun as the yellow dot (Lodders et al. 2009). The metallicity axis is normalized to the solar values (see Equation (2)).

measured n_O is scaled upward by 40%, we indeed obtain a lower $C/O = 0.45^{+0.08}_{-0.10}$ and a slightly higher $[M/H] = 1.17^{+0.66}_{-1.01}$ (Figure 8, green dotted lines). Even with this correction, the chemistry derived from the free retrieval is incompatible with the parent star at $\geqslant 2\sigma$.

Furthermore, with dissociation processes one should expect strongly altitude-dependent gas mixing ratio profiles (Lothringer et al. 2018; Parmentier et al. 2018). In particular, the abundance of H_2O rapidly decreases at the atmospheric pressures where dissociation begins, with a corresponding increase in the OH abundance, which is indeed visible in the 1D-RCTE models shown in Figures 3 and 6. To counterbalance this effect, the constant-with-altitude retrieval models assumed here will attempt to compensate by adjusting the absolute abundances, changing the lapse rate (through the γ_V parameter), or shift the overall TP profile (through the κ_{IR} parameter). These adjustments defy simple intuition, due to the known correlation between abundances and lapse rate, as well as to the saturation of strong CO and OH line cores forming in the upper isothermal layer.

Finally, all free retrievals must assume a "filler gas," e.g., H_2O, OH, and CO are all trace gases and the remaining is some mixture of H_2, He, and atomic H; however, we do not know their relative proportions as we have little sensitivity to the hydrogen-induced continua. All in all, we suspect that absolute abundances from the "free-chemistry" retrieval might be biased due to the shortcomings of our current modeling, impacting the accuracy of the elemental abundance estimates. We note, however, that these free-retrieval assumptions are valid for the WASP-77 Ab analysis of Line et al. (2021) as that planet lies within a more suitable temperature regime (e.g., no thermal dissociation, relatively constant with altitude abundances for the dominant C and O species).

In the following section, we quantitatively address these issues by building a modeling framework capable of self-consistently computing the TP and gas volume mixing ratio profiles through a grid of 1D-RCTE models.

5.2. Self-consistent Grid-based Retrieval: "Gridtrieval"

Instead of retrieving for the individual gas volume mixing ratios and a parameterized temperature profile, we fit directly for a redistribution, metallicity, and C/O derived from 1D-RCTE model fits. As a reminder, within the 1D-RCTE models, the temperature and gas vertical mixing profiles are self-consistently computed given the elemental abundances and stellar irradiation. To do this, we first build a grid of 5600 WASP-18 b 1D-RCTE models as a function of redistribution (1.85–2.65, equivalent of irradiation temperatures of 2800–3060 K in 20 K steps), [M/H] (−1.0 to 2.0, 0.125 dex increments), and C/O (0.1–0.95, 14 points with with variable spacing). Here, metallicity (or rather $10^{[M/H]}$) is a rescaling factor to the elemental abundances relative to H (Lodders et al. 2009) and C/O adjusts the relative C and O while preserving their sum after adjusting the total metallicity. We then replace our free-retrieval forward model (all other aspects remain the same) with a grid of high-resolution spectra (with the relevant opacities) generated from the 1D-RCTE model atmospheres and fit for these three "grid" parameters, along with the usual velocities and scale factor. A nearest-neighbor search is used to identify the closest [redistribution, [M/H], C/O] point for a given `pymultinest` live point parameter set.

The results of this analysis are shown in Figure 18 in Appendix C (which also illustrates the grid point spacing—sufficiently sampled to resolve the posterior shape/uncertainties), and the posteriors in C/O and [M/H] in Figure 8. This method gives a $C/O < 0.34$ (2σ upper limit) and $[M/H] = 0.48^{+0.33}_{-0.29}$. The redistribution parameter constraints run up against the prior upper limit value of 2.65 (effectively the maximum physically allowed value). Similar to free-retrieval-derived temperatures, these data are unable to place a bounded constraint on the absolute temperature information. However, in contrast to the free retrievals, we do not see a noticeable degeneracy between the temperature information and composition (perhaps a slight correlation between C/O and redistribution).

Inspecting Figure 8 we find that there is no overlap in the elemental abundance constraints derived from the free and 1D-RCTE grid retrievals at better than the 2σ level. While the marginalized metallicities are consistent ($0.48^{+0.33}_{-0.29}$ versus $1.03^{+0.65}_{-1.01}$), the C/Os are vastly different, with the grid retrieval preferring C/O ratios below ∼0.3 and the free retrieval indicating C/O ratios >0.5. Correcting (green contours in Figure 8) for the "missing O" in the free retrievals helps some, but does not completely remedy the disagreement. Figure 9 elucidates an additional potential cause of these discrepancies. While the ensemble of reconstructed 1D-RCTE atmospheric profiles generally falls within the 95% CIs of the "Fiducial" free-retrieval constraints, the latter contains more flexible composition combinations as the free retrievals are not bound by 1D-RCTE.

The elevated C/O in the free retrievals is being driven by the elevated CO abundances (in Equation (1)), which are not possible over the prescribed 1D-RCTE grid dimensions and physical constraints. In a UHJ, equilibrium chemistry along an inverted TP profile results in a CO/H_2O ratio that increases

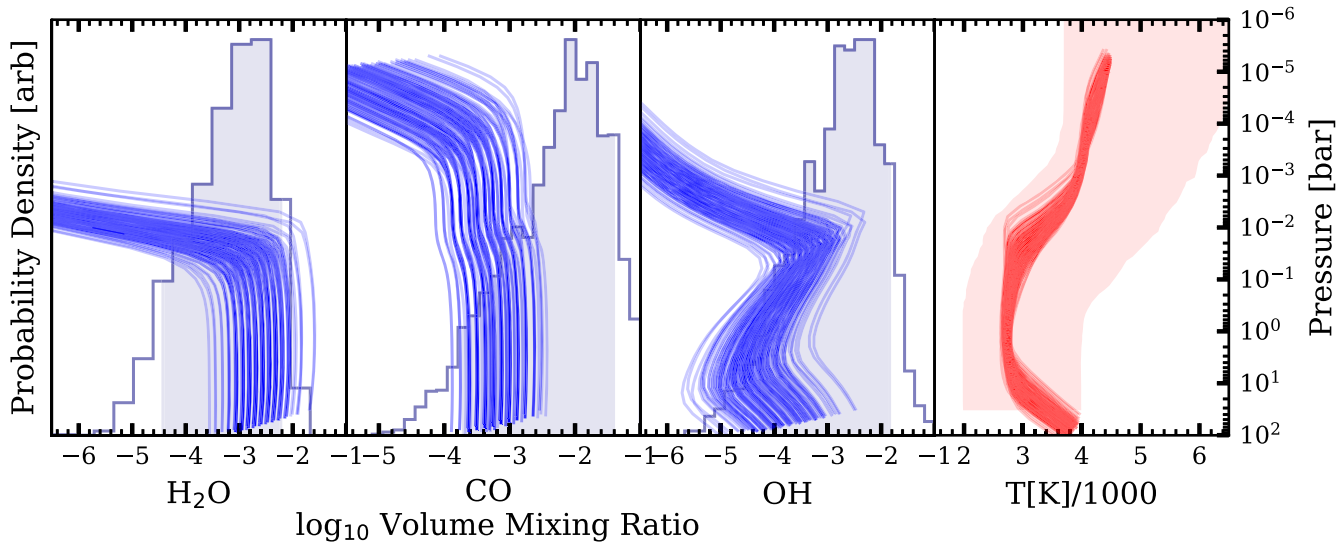

Figure 9. Grid-based retrieval gas volume mixing ratios and temperature profiles compared to the "Fiducial" free-retrieval constraints. The grid-based 1D-RCTE atmospheric gas volume mixing ratio– (left three panels in blue) and temperature– (rightmost panel in red) pressure profiles (solid curves) are drawn from the grid-retrieval posterior samples. The free-retrieval histograms and 95% CIs for H2O, CO, and OH (left 3 panels) are the same as those in the top panel of Figure 6. The rightmost panel shows the 95% CI of the reconstructed free-retrieval TP profiles in light red (same as the top left panel in Figure 7). There is general agreement in both the volume mixing ratios and temperature–pressure profiles.

with decreasing pressure due to thermal H_2O dissociation. The constant-with-altitude assumption within the free retrieval prohibits this behavior. The 1D-RCTE model cannot reproduce this high CO abundance parameter space. For instance, the 1D-RCTE CO abundance profile can be increased to the upper edge of the free-retrieval CI by increasing [M/H] to 2. However, this also increases the H_2O abundance profile beyond the free-retrieval CI. Increasing the C/O to 0.9 can reduce the H_2O abundance, however that also forces the CO abundance to go beyond the free-retrieval CI while also lowering the OH profile to fall below its free-retrieval CI. Numerous combinations of [M/H] and C/O can be manually explored, but the resulting profiles struggle to agree with the free-retrieval CIs as well as those that were indeed found by grid retrieval.

Finally, the Bayesian evidence difference between the grid-retrieval and "Fiducial" free-retrieval scenarios ($\Delta \ln Z = -1.9$) is considered weak to moderate, suggesting that there is no strong preference for one method over the other (albeit, a slight preference for the grid-based retrieval owing to the vastly reduced prior volume), meaning that the grid-based retrieval is not over-constrained relative to the free retrieval.

In summary, the grid-retrieval constraints on the redistribution, [M/H], and C/O result in temperature and vertical mixing ratio profiles that fall within the free-retrieval CIs—they are consistent. The restricted mixing ratio possibility space resulting from the imposed self-consistency from RCTE simply reduces the possible combinations of H_2O, CO, and OH. Relaxing the 1D-RCTE assumptions in the free retrievals permits higher values of CO that result in higher C/O ratios.

5.3. Are the Molecules Tracing Different Dynamics?

The single-molecule analysis presented in Section 3 reveals a tantalizing shift between the best-fit velocity solution from water vapor and those from CO and OH. We plot in Figure 10 the 1 and 2σ velocity CIs from the three species. While water vapor is approximately centered around the expected rest-frame velocity, both OH and CO appear marginally shifted.

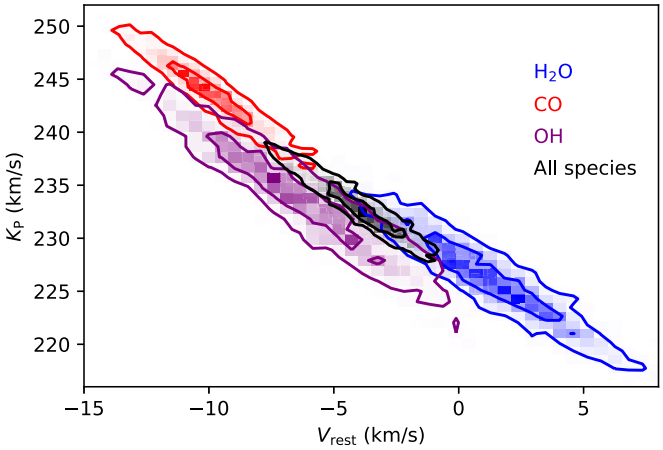

Figure 10. 1 and 2σ CIs for H_2O (blue), CO (red), OH (purple), and their mixed spectrum (black) in rest-frame velocity and planet orbital velocity. It shows a blueshift detected for CO and OH, marginally ($\sim 2\sigma$) inconsistent with H_2O. Further discussion is given in Section 5.3.

Given the final precision in the wavelength calibration of our data (better than 200 m s^{-1} for all the spectral orders), we exclude that the measured shifts are due to an imprecise instrumental calibration. Furthermore, Gandhi et al. (2020a) found that the line lists of CO and H_2O are appropriate for high-resolution studies up to $R = 100{,}000$, which excludes shifts due to inaccurate line positions. Larger line-list uncertainties for other species such as CH_4 (evident, e.g., in the T-dwarf spectra of Tannock et al. 2022) might instead impact similar velocity analyses. In our case, we also note that shifts are measured in both K_P and V_{rest}, whereas line-list inaccuracies should produce a global shift, i.e., a shift in V_{rest} only.

Doppler shifts in both K_P and V_{rest} point instead to a departure from the local "slope" of the Keplerian radial-velocity curve, which is more easily explained by invoking atmospheric circulation or heterogeneity effects. These could be due to different altitudes probed by different species, to their

emission arising from different locations on the planet disk, or to a combination of both.

In our analysis, the most evident shift is between CO and H_2O. Beltz et al. (2022) modeled the effects of magnetic drag and 3D atmospheric circulation for WASP-76 b, another UHJ. They indeed predict a differential radial velocity between two wavelength regions dominated by water (1.2 μm) and CO (2.3 μm). However, around $\varphi = 0.4$, their water appears blueshifted compared to CO, which is the opposite of our findings. Furthermore, the magnitude of their Doppler shifts is modest ($\leqslant$2 km s^{-1}) compared to our observations.

Focusing next on the milder velocity shift between OH and H_2O, this can be qualitatively explained if thermal dissociation (producing OH) mostly happens near the sub-stellar point, which is rotating toward the observer in the phase range probed by these observations (i.e., a net blueshift). Water recombines near the day–night terminator in this picture, approximately facing the observer in the observed phase range and thus showing a near-zero excess radial velocity. Building a minimal quantitative model of the above effect requires projecting the planet's synchronous equatorial rotation of 6.45 km s^{-1} along the line of sight of the observer, as well as adopting ad hoc assumptions for atmospheric circulation patterns and spatial heterogeneity in the distribution of species. We argue that such model is beyond the scope of the present study and leave it to future work.

Turning toward the evidence of similar effects in the literature, Cont et al. (2021) reported a velocity shift between TiO and Fe I from emission spectroscopy of WASP-33 b. To explain the shift, the authors tentatively invoke a TiO-depleted hot spot, but they also caution against the authenticity of the TiO signal, due to previously inconclusive searches. Sánchez-López et al. (2022) also report tentative shifts for different molecular species, this time in the infrared transmission spectrum of WASP-76 b and therefore probing the dynamics along the terminator rather than the planet's dayside. Further evidence for species-dependent dynamics starts building up when including optical transmission spectroscopy. Kesseli et al. (2022) detected a dozen different atomic species in the atmosphere of WASP-76 b and measured different velocity shifts in the K_P–V_{rest} plane. Given their high S/N, they also identified asymmetries in the time-resolved cross-correlation function, an effect that was first discovered for Fe I (Ehrenreich et al. 2020). Other searches for atoms in WASP-76 b (Tabernero et al. 2021) and WASP-189 b (Prinoth et al. 2022) also reported different shifts for different species, albeit limited to departures from the planet's V_{rest}. Lastly, Stangret et al. (2020) measured different velocity solutions for Fe I and Fe II in MASCARA-2 b (KELT-20 b), a result also obtained for the Balmer series, Na I, and Ca II (Casasayas-Barris et al. 2019).

Given the diversity of orbital phases probed (transmission versus emission spectroscopy), molecular and atomic species detected, and different irradiation regimes, it is still too soon to build a unified picture from the sparse measurements listed above. Nevertheless, the very substantial shifts of several km s^{-1} measured in WASP-18 b are potentially concerning from a modeling standpoint. The framework used here does not yet include the possibility to assign different Doppler signatures to different species, and this limit might lower the overall goodness-of-fit (i.e., the log-likelihood) of any mixed model if the true underlying spectrum has complex dynamics. One could even picture a worst-case scenario in which the retrieval, having to lock on only one velocity solution, would select that of the species with the strongest signature, thus artificially disfavoring the others. The above concern is another strong reason to search still for each species individually as done in Section 3, even with the current availability of Bayesian retrievals. In these WASP-18 b observations, it seems that mixed models are still capable of capturing three species at once with a common velocity solution (Figure 10), which is somewhat comforting.

5.4. Comparison to Past HST+Spitzer Constraints

As discussed in the introduction, Sheppard et al. (2017) concluded based upon their "free-retrieval" analysis on HST WFC3+Spitzer IRAC data, that the C/O was unity, the metallicity (via C/H) was 145–680× Solar, and that the temperature profile possessed a strong inversion. They argue that this solution is driven by the lack of a distinct water-vapor feature at 1.4 μm (driving a mixing ratio upper limit of 10^{-5}) and a high CO abundance ($\sim$20% of the total atmospheric composition) driven by the excess emission within the Spitzer IRAC 4.5 and 5.8 μm photometric channels.

In contrast, Arcangeli et al. (2018) used a 1D-RCTE grid-retrieval-based analysis on the same data and found a near-solar metallicity composition and an upper limit on the C/O $\sim$ 0.8. They argue that the lack of water features within the HST WFC3 bandpass is a natural consequence of the thermal dissociation of water and the onset of H-bound–free continuum opacity—both expected at WASP-18 b dayside temperatures.

Our results, in a way, are somewhat consistent with both Sheppard et al. (2017) and Arcangeli et al. (2018). If we just consider the CO constraints within the free-retrieval framework (similar to Sheppard et al. 2017), high-C/O and high-metallicity solutions are possible. However, owing to the higher resolution of IGRINS and coverage of an additional, stronger, water-vapor band (see Figure 3), we are able to place a constraint on the water mixing ratio—at values generally larger than the Sheppard et al. (2017) upper limit—but also we are sensitive to OH. These bounded carbon-free species constraints "dilute" the C from CO to produce C/O $<$ 1. Considering the partitioning of 40% of the oxygen into O, this reduces the C/O even further—to solar values.

Our grid-based retrieval results are most similar to Arcangeli et al. (2018)'s results. The retrieved metallicity is about a half dex higher than their retrieved median, but still falls within about 1.5σ of our solution. Their C/O upper limit contains our grid-retrieval solution. Of notable difference is the higher redistribution factor we find compared to Arcangeli et al. (2018): they find values between $\sim$2 and 2.2, fairly well-bounded, whereas the IGRINS data prefer values closer to the maximum physical redistribution upper limit (prior edge) of 2.67. However, as discussed above, the latter seems to have little influence on the retrieved elemental abundances.

6. Conclusions

In this work, we present the analysis of ground-based, high-resolution emission spectra ($R = 45{,}000$) of WASP-18 b, obtained with IGRINS at GS and a relatively modest investment of telescope time (2.85 hr). This represents the first result from our "Roasting Marshmallows" hot Jupiter survey with IGRINS. We apply state-of-the-art HRCCS

analysis techniques and learn the following about the planet's thermal and chemical properties:

1. We measure three molecular species (H_2O, CO, and OH) in cross-correlation (Section 3.1) and with the likelihood framework (Section 3.2). These are also the only three species with bounded constraints from the free retrieval (Section 4).
2. We unambiguously confirm the presence of a thermal inversion layer, via the positive correlation with 1D-RCTE models containing emission lines (Section 3.1) and via the retrieval of a strictly positive $\log(\gamma_V)$ parameter for the planet's TP profile (Section 4).
3. In contrast to emission spectroscopy of the hot Jupiter WASP-77 Ab (Line et al. 2021), we observe a strong degeneracy between the global scaling factor and the parameters describing the TP profile. Such degeneracy prevents us from obtaining meaningful constraints on the planet's irradiation temperature (Section 4). It is still unclear whether the lifting of the degeneracy in previous work was due to the much stronger detection, or due to the different irradiation regimes of the planet.
4. In spite of the above degeneracy, the retrieved absolute abundances appear robust against the value of the scaling factor across orders of magnitude.
5. We highlight the shortcomings of a "free-chemistry" model assuming constant vertical abundances and ignoring atomic oxygen to reproduce both the correct line shape and depth in the presence of thermal dissociation (Section 5.1). Such model points to a C/O of $0.75^{+0.14}_{-0.17}$ and a metallicity $[M/H] = 1.03^{+0.66}_{-1.01}$ for WASP-18 b, both higher than those of the parent star (C/O = 0.23, [M/H] = 0.05).
6. Retrieving C/O and [M/H] with a self-consistent model incorporating the TP-abundance profiles in the presence of thermal dissociation leads to C/O < 0.34 (2σ) and $[M/H] = 0.48^{+0.33}_{-0.29}$, i.e., tighter constraints in line with stellar values (Section 5.2).
7. The resulting 1D-RCTE grid-retrieval volume mixing ratio and TP profiles are in agreement with the free-retrieval 95% CIs (Section 5.2, Figure 9). The flexibility of the free retrieval allows a broad range of abundance combinations, some nonphysical, that drive the C/O to higher values.
8. We see evidence for additional Doppler shifts compared to the planet's orbital velocity as a function of molecular species, and we advocate for follow-up observations to confirm these shifts (Section 5.3).

As we develop the systematic application of HRCCS to retrieve the abundances and temperature of exoplanets robustly using infrared spectroscopy of an UHJ, we highlight a few final points relevant to future work. First, given the strong degeneracy with the TP profile, the inclusion of a $\log(a)$ parameter appears conceptually questionable. In fact, an appropriate atmospheric model should reproduce the correct line depth by adjusting the other physical parameters. On the other hand, directly fitting for $\log(a)$ allows us to diagnose potential modeling shortcomings (as in this case) when $\log(a)$ is significantly deviant from 0.

Second, UHJs require a more complex parameterization of the abundance profiles of (at least) H_2O and OH, and an estimate of the atomic oxygen produced via thermal dissociation (see also Kasper et al. 2023). This is to be implemented in future work.

Third, putting together the lessons learned from ground and space observations of WASP-18 b, we anticipate that the interpretation of JWST emission spectra of UHJs will be complex, especially if CO is weakly detectable and OH and O are not detectable. On the other hand, these spectra will not suffer from the TP profile degeneracy due to the additional continuum information retained. Overall, the combination of low-resolution and high-resolution spectroscopy is particularly appealing for this class of planets, particularly for WASP-18 b, as it is a recently observed JWST Early Release Science target (L.-P. Coulombe et al. 2023, in preparation). Continuing to validate inferences derived from high-resolution observations against those from low-resolution space-based observations from JWST will serve to identify weaknesses and areas of improvement in our model-based inferences.

Finally, as in past works we are continuing to use simplified 1D radiative-transfer forward models to retrieve intrinsically 3D objects. There are already well-known biases that can occur when interpreting low-resolution HST/JWST data with 1D models (e.g., Feng et al. 2016; Line & Parmentier 2016; Blecic et al. 2017; Taylor et al. 2020). How such biases—resulting from spatially heterogeneous compositions, temperatures, and wind fields— manifest in high-resolution data and how they can be mitigated within computationally feasible retrieval models is certainly an area worth exploring in future works as we continue to push the observational limits (as a starting point, see Beltz et al. 2021; van Sluijs et al. 2022). It is particularly exciting that we are entering a regime where data quality is sufficiently good to consider such effects. It means that there is much more information within these data sets that have yet to be exploited in order to improve our understanding of the climate and composition of highly irradiated worlds.

This work used the Immersion Grating Infrared Spectrometer (IGRINS) that was developed under a collaboration between the University of Texas at Austin and the Korea Astronomy and Space Science Institute (KASI) with the financial support of the Mt. Cuba Astronomical Foundation, of the US National Science Foundation under grants AST-1229522 and AST-1702267, of the McDonald Observatory of the University of Texas at Austin, of the Korean GMT Project of KASI, and Gemini Observatory. J.L.B., M.R.L., and P.S. acknowledge support from NASA XRP grant 80NSSC19K0293. M.B. acknowledges support from the STFC research grant ST/T000406/1. M.M. acknowledges support through NASA Hubble Fellowship grant HST-HF2-51485.001-A awarded by the Space Telescope Science Institute, which is operated by the Association of Universities for Research in Astronomy, Inc., for NASA, under contract NAS5-26555. J.L.B. acknowledges funding from the European Research Council (ERC) under the European Union's Horizon 2020 research and innovation program under grant agreement No. 805445. We would also like to thank the NOIRLabs support staff helping with the implementation of these observations. Finally, we acknowledge Research Computing at Arizona State University for providing HPC and storage resources that have significantly contributed to the research results reported within this manuscript.

Facility: Gemini-South (IGRINS).

Software: `astropy` (Astropy Collaboration et al. 2018), `barycorrpy` (Kanodia & Wright 2018), `corner`

(Foreman-Mackey 2016), `matplotlib` (Hunter 2007), `numpy` (Harris et al. 2020), `python` (Van Rossum & Drake 2009), `scipy` (Virtanen et al. 2020).

Appendix A
Robustness of the Detection to a Range of Telluric Removal Algorithms

To our knowledge, a full quantitative comparison of telluric removal algorithms has never been performed before. In Line et al. (2021), we have investigated the dependence on the number of SVD components removed, but in this study we address additional subtleties that can potentially affect the result.

To make the comparison quantitative, we select the equilibrium model containing the three detected species (H_2O, CO, OH; see Section 3) and we explore the three-parameter space in (V_{sys}, K_P, $\log(a)$) as in Section 3.2, for each of the tested analyses. The posteriors of the three parameters are then compared quantitatively to look for significant shifts in their best-fit values. Figure 11 presents a representative subset of the 120 tests we performed. We compare the SVD-only algorithm of Line et al. (2021) with the full PCA of Giacobbe et al. (2021), which contains SVD as one of the three main steps. We ran the algorithms in both the TD and wavelength domain (WD), varying the number of components between three and eight. Furthermore, we ran the telluric removal in both logarithmic and linear flux space. In the latter case, we compare subtracting the best fit to dividing through the best fit. We note that changing the flux space and correction method is equivalent to weighting the data by their relative versus absolute error.

The signal from the planet is detected in all cases, albeit the size of the CI varies, indicating that some analyses seem to be more effective at preserving the exoplanet signal than other. Furthermore, within 1σ all the versions of the analysis yield the same best-fit parameters, as shown in Figure 11. We note that this result relies on model reprocessing to be applied and modified accordingly to the type of the analysis selected, so that model and data undergo the same processing.

Incidentally, smaller CIs are obtained with the analysis presented in this study (SVD, TD, linear space, subtraction), which is also the analysis used by Line et al. (2021).

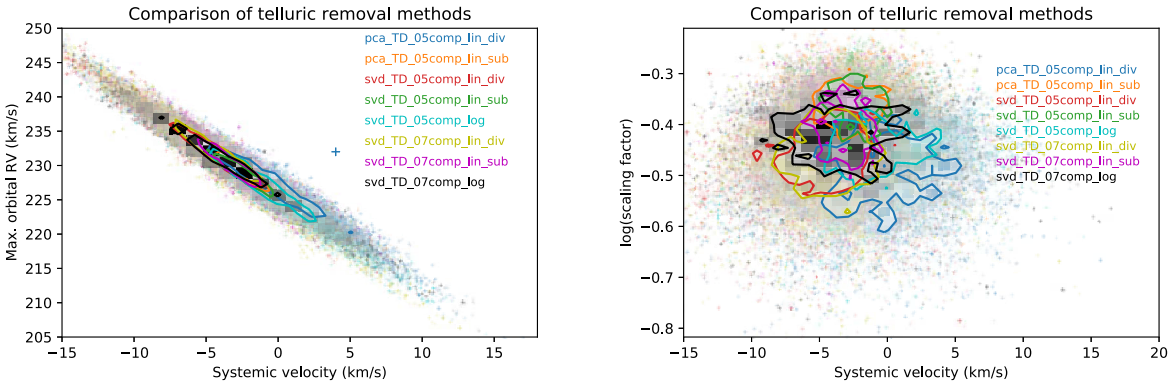

Figure 11. Posteriors in V_{sys}, K_P (left panel), and V_{sys}, $\log(a)$ (right panel) obtained by varying the telluric removal analysis. Labels encode type of analysis done (`pca` or `svd`) in the TD (`TD`), the number of components (`XXcomp`), the flux space (`lin` for linear, `log` for logarithmic), and whether the fit is divided (`div`) through the data or subtracted (`sub`) out. It shows that the best-fit parameters are unbiased within 1σ (solid contours) regardless of the subtleties of the telluric removal.

Appendix B
HyDRA-H and CHIMERA Retrieval Comparison

We benchmarked the retrieval results of CHIMERA against a retrieval performed on WASP-18 b with HyDRA-H (Gandhi et al. 2019), similarly to what we did for WASP-77 Ab in Line et al. (2021). The HyDRA-H retrieval used 13 free parameters, namely the volume mixing ratios of the chemical species H_2O, OH, CO, H-, and Ca, six free parameters to describe the temperature profile using the prescription of Madhusudhan & Seager (2009), and two parameters for velocity shifts from the expected values of K_P and V_{rest}. For the molecular and atomic cross sections we used the HITEMP database (Rothman et al. 2010) for H_2O, CO, and OH, the Kurucz database for Ca (Kurucz & Bell 1995 and Bell & Berrington 1987), and John (1988) for H (see also Gandhi et al. 2020b). Our statistical analysis was performed with the MultiNest Nested Sampling algorithm (Feroz & Hobson 2008; Feroz et al. 2009; Buchner et al. 2014). Further details of the retrieval setup can be found in Gandhi et al. (2019) and Line et al. (2021). This retrieval can be directly compared with the "Fixed $a = 1$" retrieval presented in Section 4.2 and summarized in Table 2. We note that the parameterization of the TP profile is different between the two retrievals, and therefore this is a good test to highlight the dependence of the result on the parameterization for UHJs, which might differ from the agreement measured for a hot Jupiter such as WASP-77 Ab.

The retrieved volume mixing ratios are shown in Figure 12 and show good agreement with all of the constraints from CHIMERA. We strongly constrain H_2O, OH, and CO, but only obtain an upper limit for Ca due to the weaker peak in the posterior. Our temperature profiles are also in good agreement, indicating temperatures near 3500 K for the photosphere with an inversion of ~500 K. However, there is a very slight difference in the temperature gradient, where the HyDRA-H retrievals constrain a shallower inversion, which requires a slightly higher abundance of the chemical species to fit the spectrum. However, these differences in the temperature structure and abundances are well within the 1σ error bars of each of the retrievals, and the overall agreement between the two different models remains excellent.

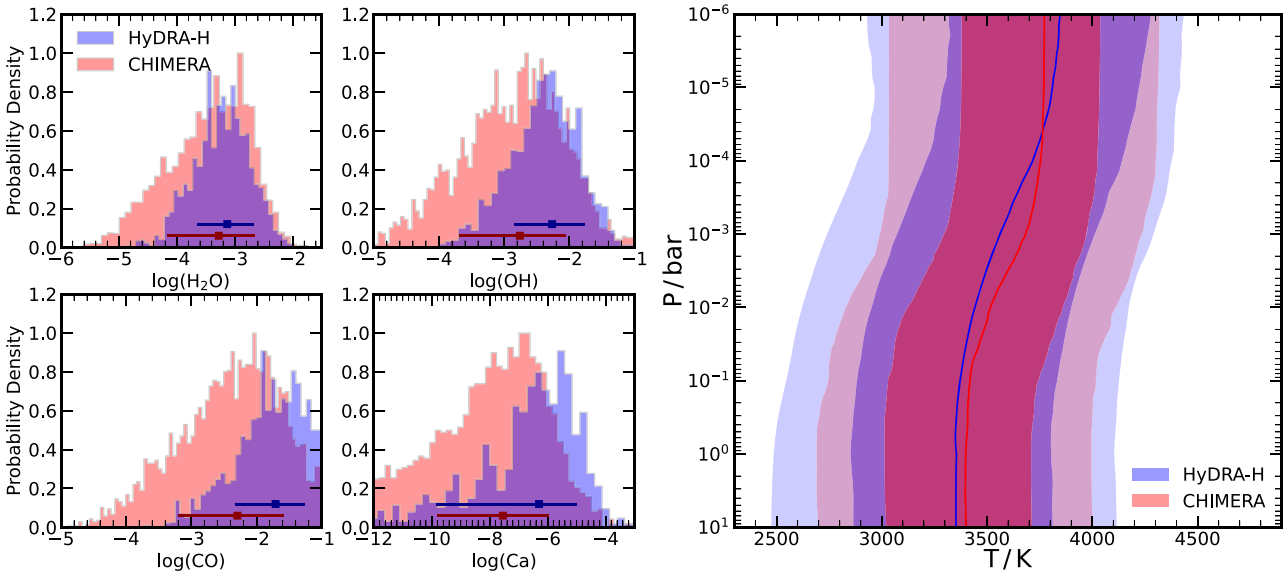

Figure 12. Comparison between the HyDRA-H retrieval (in blue) and the "Fixed $a = 1$" CHIMERA retrieval (in red; see also Table 2 and Section 4.2). The constraints on the abundances (four panels, left side) and the TP profiles (right side) are compatible within 1σ.

Appendix C
Corner Plots from the Five Retrievals of WASP-18 b

In this section we provide the full corner plots obtained from the five retrieval runs described in Section 4, as well as the full corner plot for the grid retrieval described in Section 5.2.

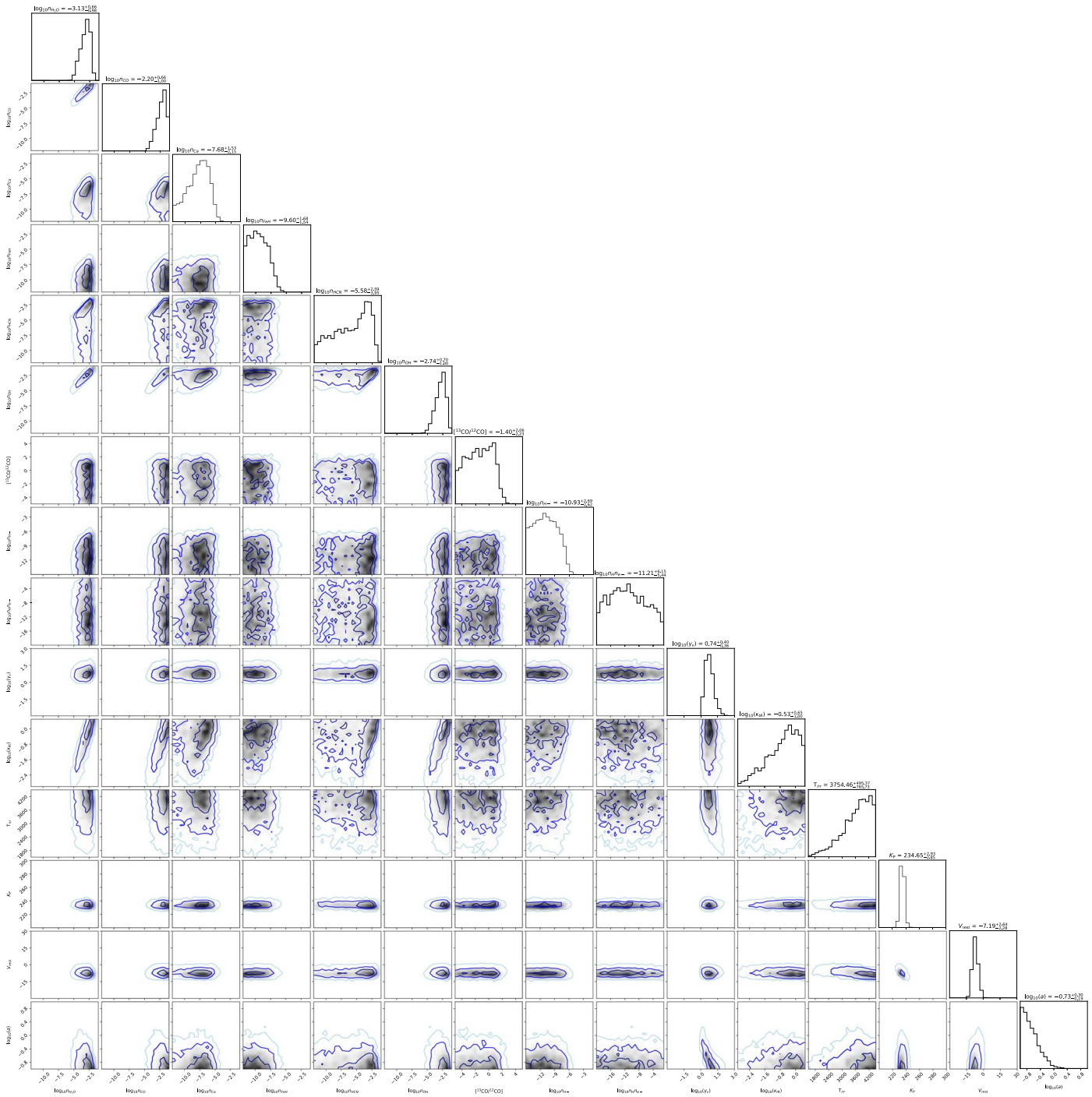

Figure 13. Corner plots for the 15 parameters of the "Fiducial" retrieval including a scaling factor. See Section 4 for details.

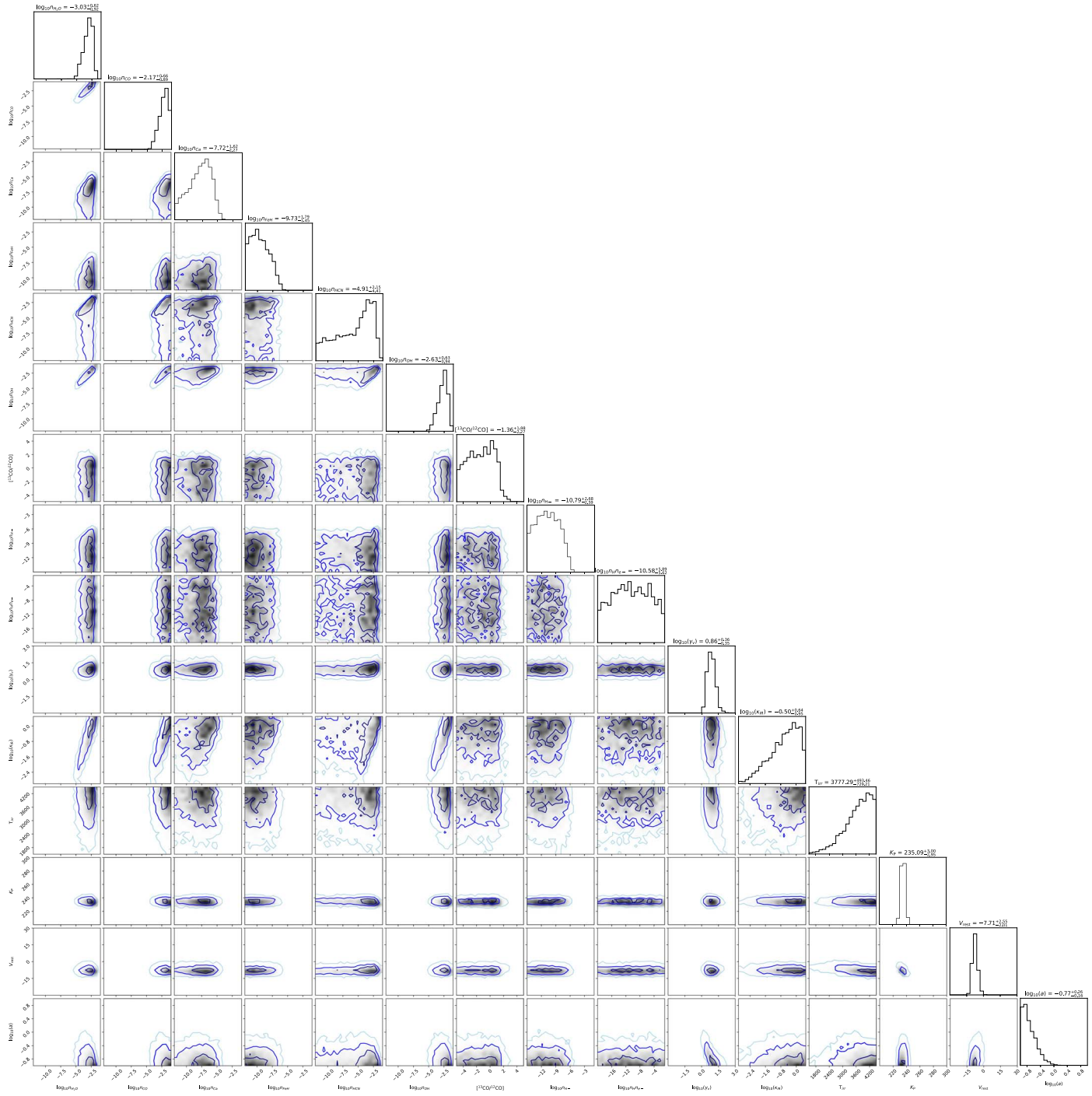

Figure 14. Corner plots for the 15 parameters of the retrieval where a cosine function is applied to the scaling factor as a function of planet orbital phase (labeled as "Phase Dep. a" in Table 2). See Section 4.2 for details.

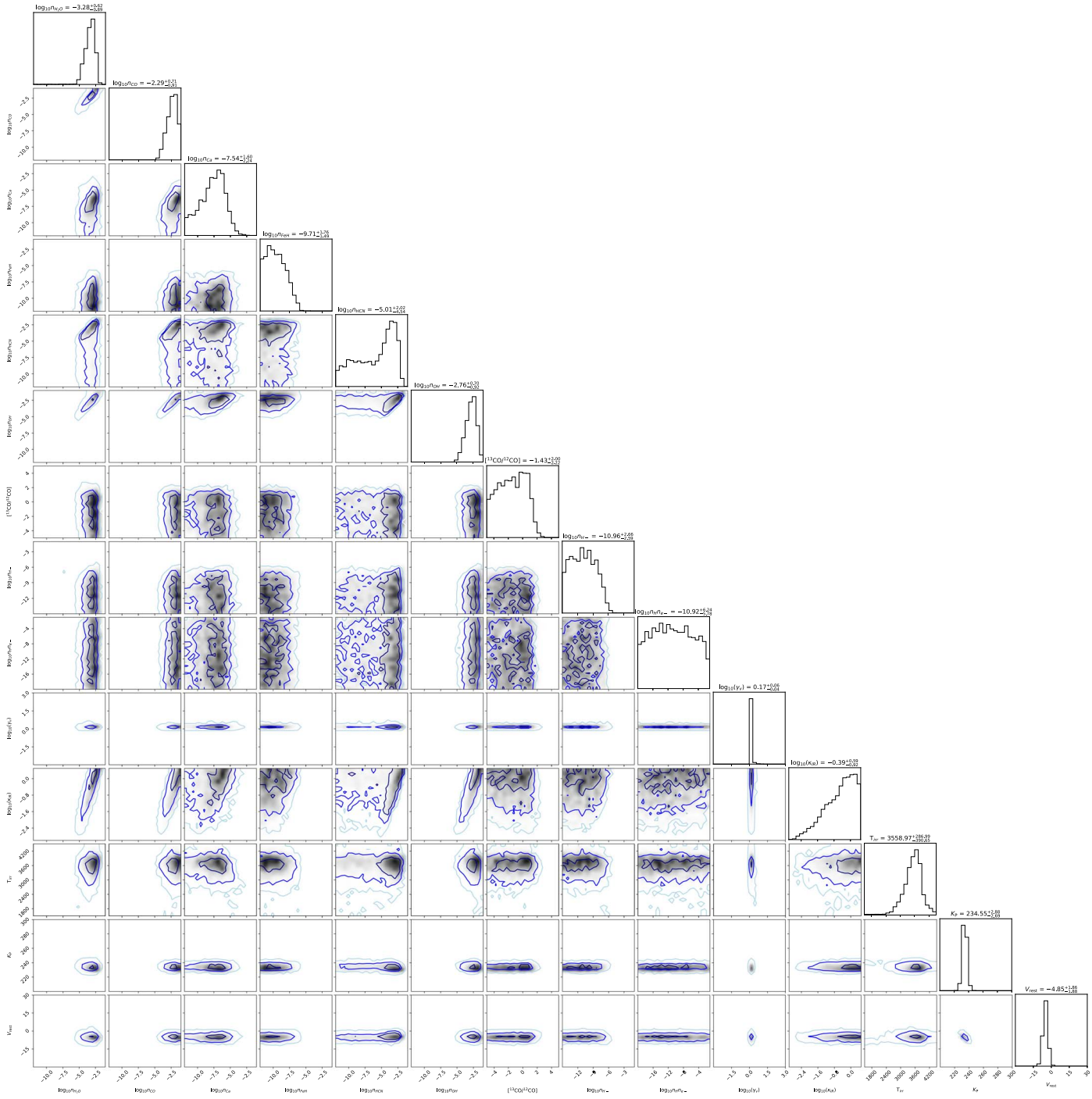

Figure 15. Corner plots for the 14 parameters of the retrieval with the scaling factor set to 1 (labeled as "Fixed $a = 1$" in Table 2). See Section 4.2 for details.

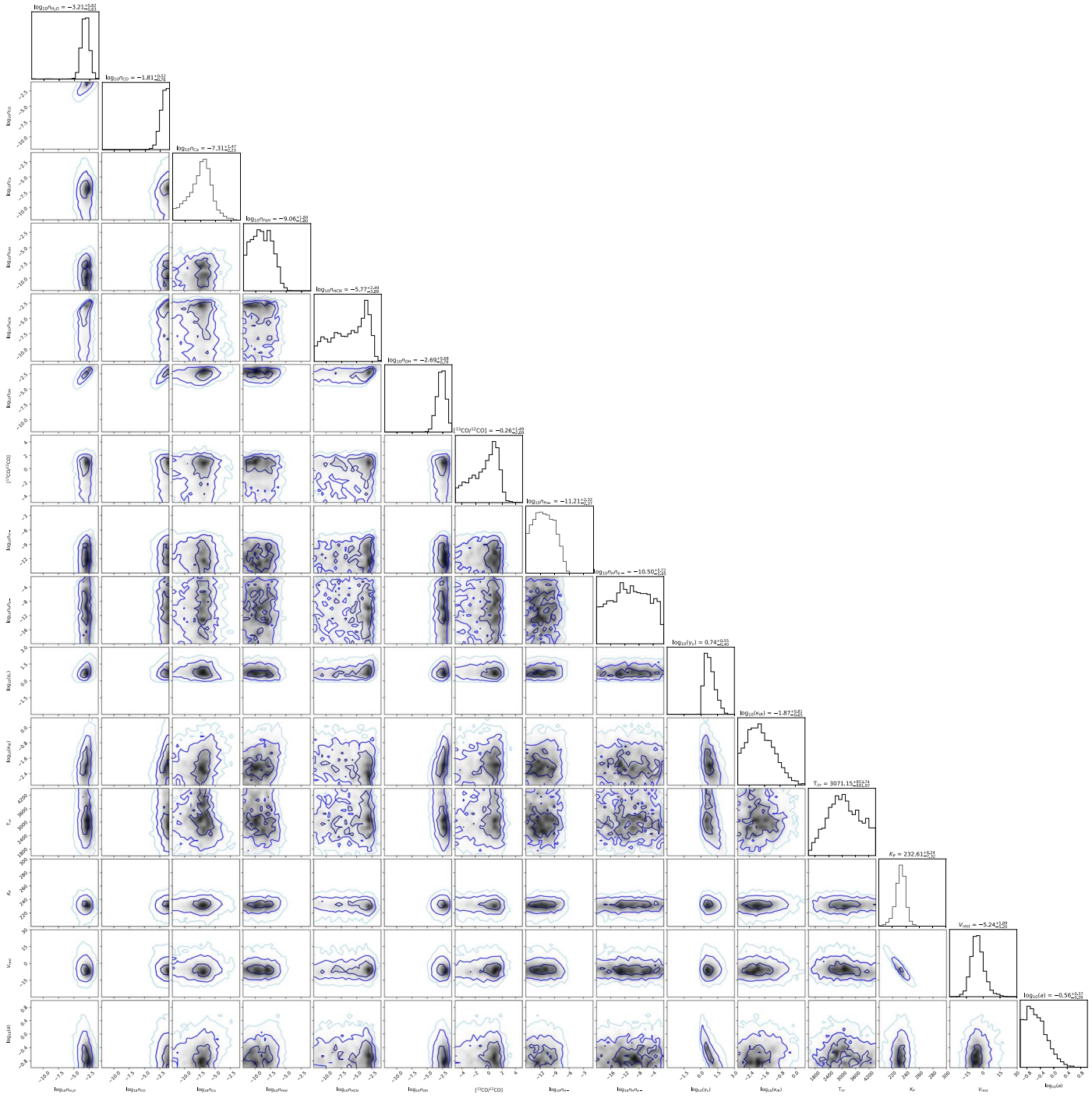

Figure 16. Corner plots for the 15 parameters of the retrieval including only the first half of the spectra (labeled as "1st half" in Table 2). See Section 4.3 for details.

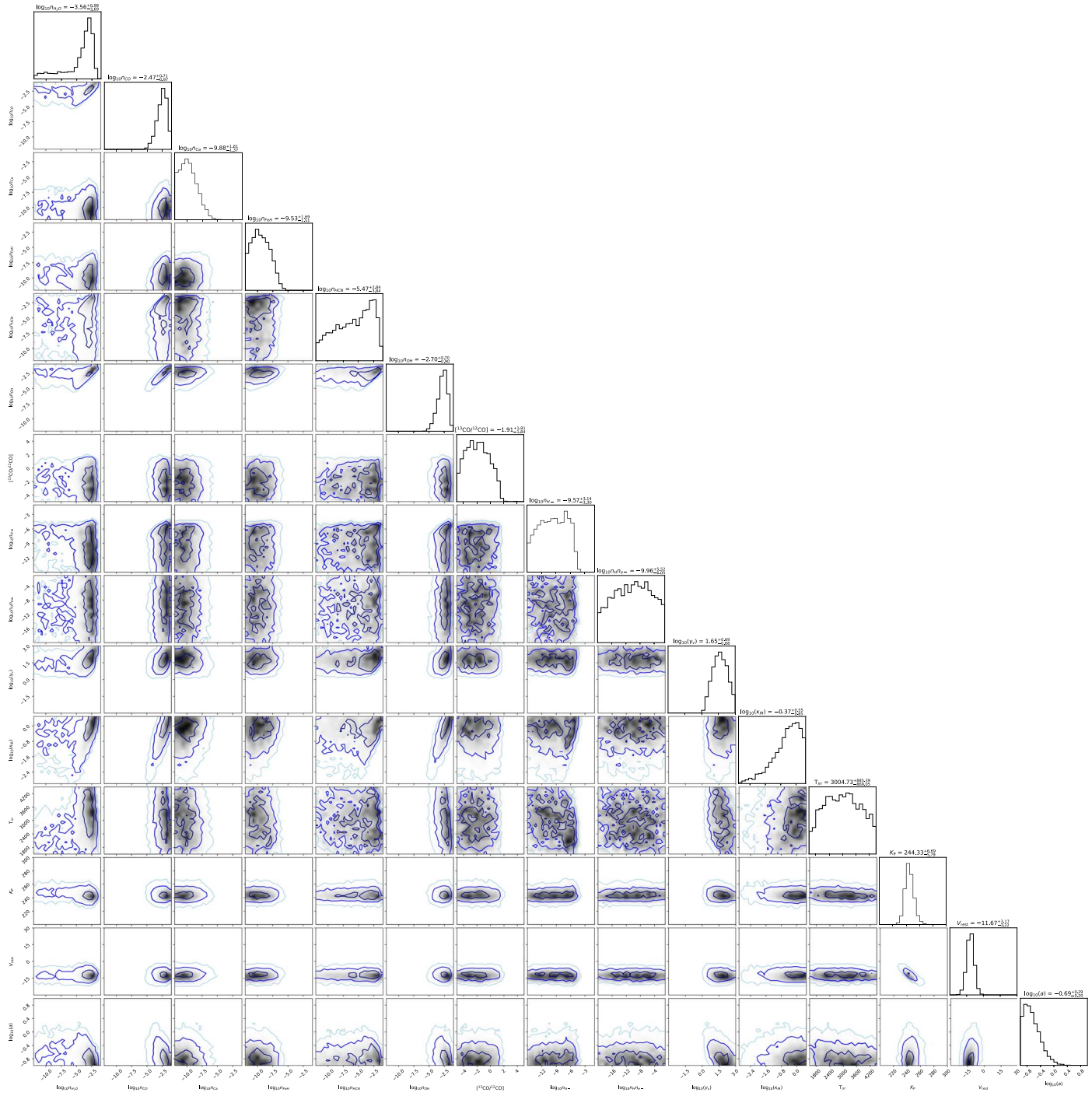

Figure 17. Corner plots for the 15 parameters of the retrieval including only the second half of the spectra (labeled as "2nd half" in Table 2). See Section 4.3 for details.

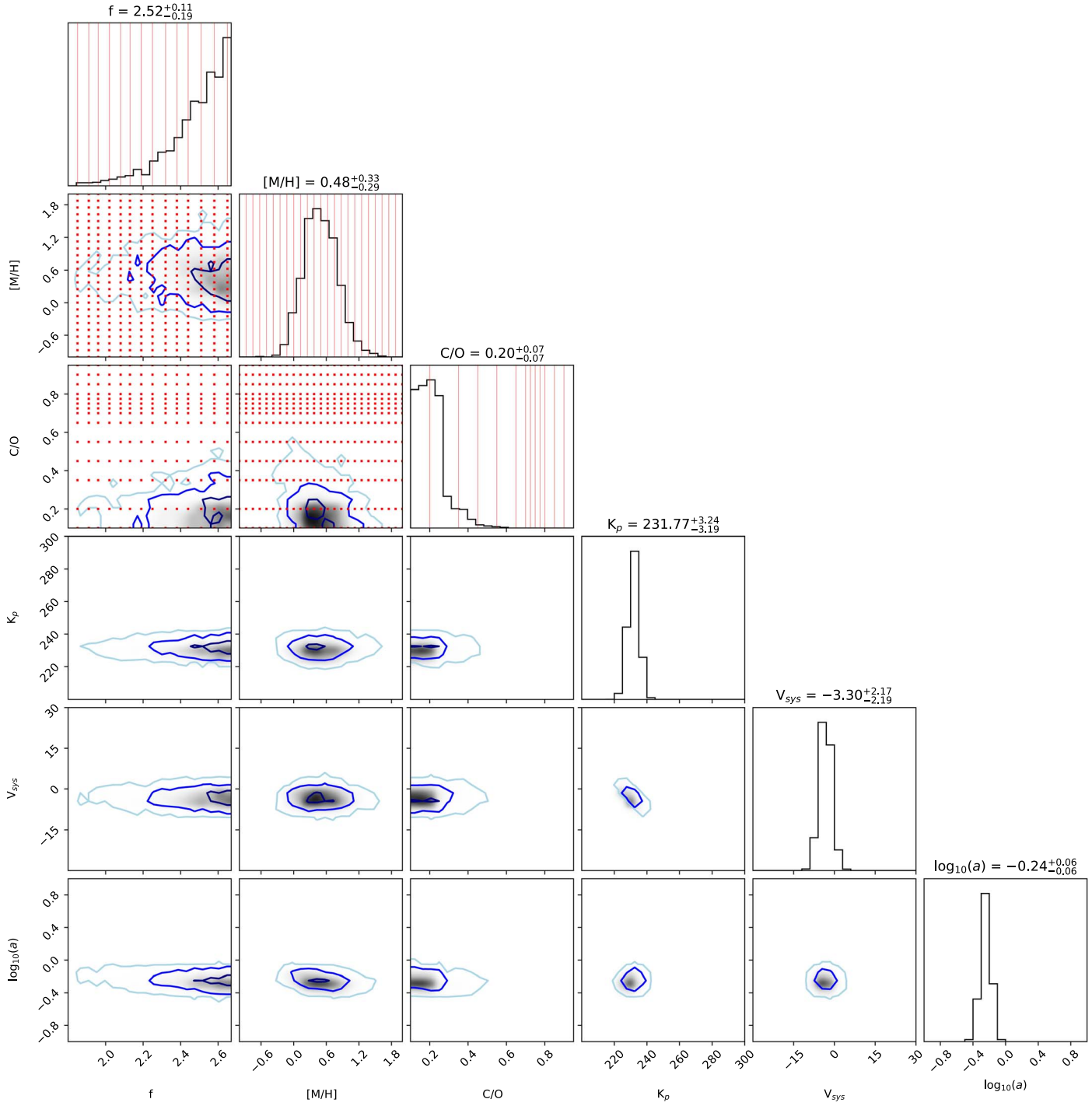

Figure 18. Corner plot for the six parameters of the grid retrieval including a scaling factor. The red dots mark the grid points corresponding to each of the computed 1D-RCTE models. The same grid points are marked for each parameter as solid red lines in the marginalized posteriors. It is apparent that the grid points are sampled finely enough to resolve the posterior shape. See Section 5.2 for details.

ORCID iDs

Matteo Brogi https://orcid.org/0000-0002-7704-0153
Michael R. Line https://orcid.org/0000-0002-2338-476X
Siddharth Gandhi https://orcid.org/0000-0001-9552-3709
Lorenzo Pino https://orcid.org/0000-0002-1321-8856
Eliza M.-R. Kempton https://orcid.org/0000-0002-1337-9051
Emily Rauscher https://orcid.org/0000-0003-3963-9672
Jacob L. Bean https://orcid.org/0000-0003-4733-6532
Gregory N. Mace https://orcid.org/0000-0001-7875-6391
Nicolas B. Cowan https://orcid.org/0000-0001-6129-5699
Evgenya Shkolnik https://orcid.org/0000-0002-7260-5821
Joost P. Wardenier https://orcid.org/0000-0003-3191-2486
Luis Welbanks https://orcid.org/0000-0003-0156-4564
Peter Smith https://orcid.org/0000-0002-9946-5259
Jonathan J. Fortney https://orcid.org/0000-0002-9843-4354
Jayne L. Birkby https://orcid.org/0000-0002-4125-0140
Joseph A. Zalesky https://orcid.org/0000-0002-2259-4116
Lisa Dang https://orcid.org/0000-0003-4987-6591
Jean-Michel Désert https://orcid.org/0000-0002-0875-8401

References

Arcangeli, J., Désert, J.-M., Line, M. R., et al. 2018, ApJL, 855, L30
Arcangeli, J., Désert, J.-M., Parmentier, V., et al. 2019, A&A, 625, A136
Astropy Collaboration, Price-Whelan, A. M., Sipőcz, B. M., et al. 2018, AJ, 156, 123
Barber, R. J., Strange, J. K., Hill, C., et al. 2013, MNRAS, 437, 1828
Baxter, C., Désert, J.-M., Parmentier, V., et al. 2020, A&A, 639, A36
Bean, J. L., Stevenson, K. B., Batalha, N. M., et al. 2018, PASP, 130, 114402
Bedell, M., Bean, J. L., Meléndez, J., et al. 2018, ApJ, 865, 68
Bell, K. L., & Berrington, K. A. 1987, JPhB, 20, 801
Beltz, H., Rauscher, E., Brogi, M., & Kempton, E. M. R. 2021, AJ, 161, 1
Beltz, H., Rauscher, E., Kempton, E. M. R., et al. 2022, AJ, 164, 140
Bernath, P. F. 2020, JQSRT, 240, 106687
Birkby, J. L. 2018, Handbook of Exoplanets (Cham: Springer)
Blecic, J., Dobbs-Dixon, I., & Greene, T. 2017, ApJ, 848, 127
Brewer, J. M., & Fischer, D. A. 2016, ApJ, 831, 20
Brogi, M., & Birkby, J. 2021, in ExoFrontiers; Big Questions in Exoplanetary Science, ed. N. Madhusudhan (Bristol: IOP), 8
Brogi, M., & Line, M. R. 2019, AJ, 157, 114
Buchner, J., Georgakakis, A., Nandra, K., et al. 2014, A&A, 564, A125
Burrows, A., Sudarsky, D., & Hubeny, I. 2006, ApJ, 650, 1140
Casasayas-Barris, N., Pallé, E., Yan, F., et al. 2019, A&A, 628, A9
Cont, D., Yan, F., Reiners, A., et al. 2021, A&A, 651, A33
Cowan, N. B., & Agol, E. 2011, ApJ, 729, 54
de Kok, R. J., Brogi, M., Snellen, I. A. G., et al. 2013, A&A, 554, A82
Ehrenreich, D., Lovis, C., Allart, R., et al. 2020, Natur, 580, 597
Feng, Y. K., Line, M. R., Fortney, J. J., et al. 2016, ApJ, 829, 52
Feroz, F., & Hobson, M. P. 2008, MNRAS, 384, 449
Feroz, F., Hobson, M. P., & Bridges, M. 2009, MNRAS, 398, 1601
Foreman-Mackey, D. 2016, JOSS, 1, 24
Fortney, J. J. 2012, ApJL, 747, L27
Fortney, J. J., Lodders, K., Marley, M. S., & Freedman, R. S. 2008, ApJ, 678, 1419
Fortney, J. J., Marley, M. S., Lodders, K., Saumon, D., & Freedman, R. 2005, ApJL, 627, L69
Gaia Collaboration, Brown, A. G. A., Vallenari, A., et al. 2018, A&A, 616, A1
Gandhi, S., Brogi, M., Yurchenko, S. N., et al. 2020a, MNRAS, 495, 224
Gandhi, S., Madhusudhan, N., Hawker, G., & Piette, A. 2019, AJ, 158, 228
Gandhi, S., Madhusudhan, N., & Mandell, A. 2020b, AJ, 159, 232
Gharib-Nezhad, E., Iyer, A. R., Line, M. R., et al. 2021, ApJS, 254, 34
Giacobbe, P., Brogi, M., Gandhi, S., et al. 2021, Natur, 592, 205
Gordon, I., Rothman, L., Hargreaves, R., et al. 2022, JQSRT, 277, 107949
Grevesse, N., Asplund, M., & Sauval, A. J. 2007, SSRv, 130, 105
Grimm, S. L., Malik, M., Kitzmann, D., et al. 2021, ApJS, 253, 30
Guillot, T. 2010, A&A, 520, A27
Guillot, T., Fletcher, L. N., Helled, R., et al. 2022, arXiv:2205.04100
Harris, C. R., Millman, K. J., van der Walt, S. J., et al. 2020, Natur, 585, 357
Hellier, C., Anderson, D. R., Collier Cameron, A., et al. 2009, Natur, 460, 1098
Hubeny, I., Burrows, A., & Sudarsky, D. 2003, ApJ, 594, 1011
Hunter, J. D. 2007, CSE, 9, 90
Iro, N., Bézard, B., & Guillot, T. 2005, A&A, 436, 719
John, T. L. 1988, A&A, 193, 189
Kanodia, S., & Wright, J. 2018, RNAAS, 2, 4
Kasper, D., Bean, J. L., Line, M. R., et al. 2021, ApJL, 921, L18
Kasper, D., Bean, J. L., Line, M. R., et al. 2023, AJ, 165, 11
Kempton, E. M.-R., Bean, J. L., & Parmentier, V. 2017, ApJL, 845, L20
Kesseli, A. Y., Snellen, I. A. G., Casasayas-Barris, N., Mollière, P., & Sánchez-López, A. 2022, AJ, 163, 107
Kolecki, J. R., & Wang, J. 2022, AJ, 164, 87
Kreidberg, L., Line, M. R., Bean, J. L., et al. 2015, ApJ, 814, 66
Kurucz, R. L., & Bell, B. 1995, Atomic Line List (Cambridge, MA: Smithsonian Astrophysical Observatory), CD-ROM No. 23
Lee, J.-J., & Gullikson, K. 2016, Plp: V2.1 Alpha 3, v2.1-alpha.3, Zenodo, doi:10.5281/zenodo.56067
Line, M. R., Brogi, M., Bean, J. L., et al. 2021, Natur, 598, 580
Line, M. R., Knutson, H., Deming, D., Wilkins, A., & Desert, J.-M. 2013, ApJ, 778, 183
Line, M. R., & Parmentier, V. 2016, ApJ, 820, 78
Line, M. R., Teske, J., Burningham, B., Fortney, J. J., & Marley, M. S. 2015, ApJ, 807, 183
Lodders, K., Palme, H., & Gail, H.-P. 2009, Solar System (Berlin: Springer), 712
Lothringer, J. D., Barman, T., & Koskinen, T. 2018, ApJ, 866, 27
Mace, G., Sokal, K., Lee, J.-J., et al. 2018, Proc. SPIE, 10702, 107020Q
Madhusudhan, N. 2018, in Handbook of Exoplanets, ed. H. J. Deeg & J. A. Belmonte (Cham: Springer), 104
Madhusudhan, N. 2019, ARA&A, 57, 617
Madhusudhan, N., Crouzet, N., McCullough, P. R., Deming, D., & Hedges, C. 2014, ApJL, 791, L9
Madhusudhan, N., Mousis, O., Johnson, T. V., & Lunine, J. I. 2011, ApJ, 743, 191
Madhusudhan, N., & Seager, S. 2009, ApJ, 707, 24
Mansfield, M., Line, M. R., Bean, J. L., et al. 2021, NatAs, 5, 1224
Maxted, P. F. L., Anderson, D. R., Doyle, A. P., et al. 2013, MNRAS, 428, 2645
Nymeyer, S., Harrington, J., Hardy, R. A., et al. 2011, ApJ, 742, 35
Park, C., Jaffe, D. T., Yuk, I.-S., et al. 2014, Proc. SPIE, 9147, 91471D
Parmentier, V., Line, M. R., Bean, J. L., et al. 2018, A&A, 617, A110
Parmentier, V., Showman, A. P., & Fortney, J. J. 2021, MNRAS, 501, 78
Perez-Becker, D., & Showman, A. P. 2013, ApJ, 776, 134
Piette, A. A. A., & Madhusudhan, N. 2020, MNRAS, 497, 5136
Piskorz, D., Buzard, C., Line, M. R., et al. 2018, AJ, 156, 133
Polanski, A. S., Crossfield, I. J. M., Howard, A. W., Isaacson, H., & Rice, M. 2022, RNAAS, 6, 155
Polyansky, O. L., Kyuberis, A. A., Zobov, N. F., et al. 2018, MNRAS, 480, 2597
Prinoth, B., Hoeijmakers, H. J., Kitzmann, D., et al. 2022, NatAs, 6, 449
Rothman, L. S., Gordon, I. E., Barber, R. J., et al. 2010, JQSRT, 111, 2139
Sánchez-López, A., Landman, R., Mollière, P., et al. 2022, A&A, 661, A78
Seager, S. 2010, Exoplanet Atmospheres: Physical Processes (Princeton, NJ: Princeton University Press)
Sheppard, K. B., Mandell, A. M., Tamburo, P., et al. 2017, ApJL, 850, L32
Shporer, A., Wong, I., Huang, C. X., et al. 2019, AJ, 157, 178
Sing, D. K., Fortney, J. J., Nikolov, N., et al. 2016, Natur, 529, 59
Snellen, I. A. G., de Kok, R. J., de Mooij, E. J. W., & Albrecht, S. 2010, Natur, 465, 1049
Stangret, M., Casasayas-Barris, N., Pallé, E., et al. 2020, A&A, 638, A26
Tabernero, H. M., Zapatero Osorio, M. R., Allart, R., et al. 2021, A&A, 646, A158
Tannock, M. E., Metchev, S., Hood, C. E., et al. 2022, MNRAS, 514, 3160
Taylor, J., Parmentier, V., Line, R. M., et al. 2021, MNRAS, 506, 1309
Tennyson, J., Yurchenko, S. N., Al-Refaie, A. F., et al. 2020, JQSRT, 255, 107228
Thorngren, D. P., Fortney, J. J., Murray-Clay, R. A., & Lopez, E. D. 2016, ApJ, 831, 64
Trotta, R. 2008, ConPh, 49, 71
Van Rossum, G., & Drake, F. L. 2009, Python 3 Reference Manual (Scotts Valley, CA: CreateSpace)
van Sluijs, L., Birkby, J. L., Lothringer, J., et al. 2022, arXiv:2203.13234
Virtanen, P., Gommers, R., Oliphant, T. E., et al. 2020, NatMe, 17, 261
Welbanks, L., Madhusudhan, N., Allard, N. F., et al. 2019, ApJL, 887, L20
Wong, I., Shporer, A., Daylan, T., et al. 2020, AJ, 160, 155
Zhang, X. 2020, RAA, 20, 099